Gas metallicity of ram-pressure-stripped galaxies at intermediate redshifts with MUSE data

A. Khoram, B. Poggianti, A. Moretti, B. Vulcani, M. Radovich, A. Werle, M. Gullieuszik, J. Richard

A&A, 686, A261 (2024)
https://doi.org/10.1051/0004-6361/202348139

Astronomy & Astrophysics

Gas metallicity of ram-pressure-stripped galaxies at intermediate redshifts with MUSE data

A. Khoram[1,2], B. Poggianti[2], A. Moretti[2], B. Vulcani[2], M. Radovich[2], A. Werle[2], M. Gullieuszik[2], and J. Richard[3]

[1] Dipartimento di Fisica e Astronomia "G. Galilei", Università degli Studi di Padova, Via Marzolo 8, 35131 Padova, Italy
e-mail: amirhkhoram@gmail.com
[2] INAF-Osservatorio Astronomico di Padova, Vicolo dell'Osservatorio 5, 35122 Padova, Italy
[3] Univ. Lyon, Univ. Lyon1, ENS de Lyon, CNRS, Centre de Recherche Astrophysique de Lyon UMR5574, 69230 Saint-Genis-Laval, France

Received 3 October 2023 / Accepted 19 February 2024

ABSTRACT

Extraplanar tails of ionized-stripped gas, extending up to several tens of kiloparsecs beyond the stellar disk, are often observed in ram-pressure-stripped (RPS) galaxies in low-redshift clusters. Recent studies have also identified similar tails at high redshifts, and we present here the first analysis of the chemical composition of such tails beyond the local Universe. Specifically, we examined the distribution of the ionized gas metallicity of RPS galaxies in the Abell 2744 ($z = 0.308$) and Abell 370 ($z = 0.375$) clusters observed as part of the MUSE-GTO program. We investigated spatially resolved and global metallicities in galactic disks and stripped tails, utilizing both a theoretical calibration from a photoionization model and an empirical calibration. The metallicity gradients and the spatially resolved mass–metallicity relations indicate that the metallicity in the tails reaches values that are up to ~0.6 dex lower than anywhere in the parent disks, with a few exceptions. Both the disks and tails follow a global mass–metallicity relation, though the tail metallicity is systematically lower than that of the corresponding disk, by up to ~0.2 dex. These findings demonstrate that additional processes are at play in the tails and are consistent with a scenario of a progressive dilution of the metallicity along the tails due to the mixing of the intracluster medium and interstellar gas, in accordance with previous low-z results. In principle, the same scenario can also explain the flat or positive metallicity gradients observed in low-mass RPS galaxies since in these galaxies the interstellar medium's metallicity can approach the metallicity levels found in the intracluster medium.

Key words. ISM: abundances – HII regions – galaxies: abundances – galaxies: clusters: intracluster medium – galaxies: evolution – galaxies: ISM

1. Introduction

The hot intracluster medium (ICM) can exert ram pressure on the interstellar medium (ISM; Gunn & Gott 1972) of galaxies within massive dark matter haloes, effectively stripping gas from them. This process is regarded as the most significant physical factor shaping the gas properties of cluster galaxies (Boselli & Gavazzi 2006). There are numerous examples of ram-pressure-stripped (RPS) galaxies in clusters, including the most extreme cases, dubbed jellyfish galaxies (e.g., Fumagalli et al. 2014; Poggianti et al. 2016).

Several observational studies of the local Universe have investigated the characteristics of the gas that has been stripped from galaxies (e.g., Boselli et al. 2014; Jáchym et al. 2017; Poggianti et al. 2019b; Tomičić et al. 2021; Bacchini et al. 2023). They have revealed a diverse gas composition, from radio emission (Ignesti et al. 2023), neutral hydrogen (Chung et al. 2009), and molecular gas (Moretti et al. 2020) to X-ray-emitting gas (Sun et al. 2010). The majority of these galaxies exhibit elongated and distorted tails of ionized gas that were stripped up to several tens of kiloparsecs from the galaxy as they moved through the ICM (e.g., Poggianti et al. 2019a). The extent of the stripping can vary depending on the properties of the galaxy, such as its velocity, mass, and inclination with respect to the ICM, as well as the density and pressure of the ICM (Gullieuszik et al. 2020).

Understanding the properties and behavior of the ionized gas in RPS galaxies is essential to unraveling the complex interplay between galaxies and their environments. One key aspect essential for comprehending the nature of gas within galaxies is the gas-phase metallicity (i.e., $12 + \log(\mathrm{O/H})$). The gas-phase metallicity within the disk and along the stripped gas tail of such galaxies provides valuable insights into the interaction between the ISM and ICM during ram-pressure stripping. To date, the investigation of chemical compositions in RPS galaxies has been chiefly constrained to a handful of studies (Fossati et al. 2016; Gullieuszik et al. 2017; Moretti et al. 2018; Bellhouse et al. 2019; Franchetto et al. 2020, 2021a) conducted exclusively within the confines of the local Universe ($z < 0.1$). For example, within the GAs Stripping Phenomena in galaxies with MUSE (GASP; Poggianti et al. 2017) project, Franchetto et al. (2021b) used the Multi Unit Spectroscopic Explorer (MUSE) emission line data and a grid of photoionization models to derive the gas metallicity of three massive RPS galaxies ($M_\star > 10^{10.95}\ M_\odot$) at redshift ~0.05. The analyzed galaxy sample exhibited a steady reduction in metallicity within the tails as the distance from the galactic center increased. These findings led the authors to propose that the mixing of the ISM

and ICM is an essential process, corroborating the predictions made by simulations (Tonnesen & Bryan 2021).

The gas-phase metallicity is also considered a good tracer of the global galaxy properties. In fact, a significant area of research has been dedicated to gaining insights into the correlation between the global metallicity and other characteristics of galaxies (e.g., Tremonti et al. 2004; Hoopes et al. 2007; Mannucci et al. 2010; Hughes et al. 2013). Considerable attention has been given to the mass–metallicity relation (MZR), the strong correlation between galaxy stellar mass and gas-phase oxygen abundance, by analyzing samples of star-forming galaxies at different redshifts (ranging from 0 to ∼10). The MZR of galaxies serves as a key empirical constraint for models of galactic evolution that try to explain how galaxies form throughout cosmic time. Noteworthy studies have contributed to this body of knowledge (e.g., Tremonti et al. 2004; Kewley & Ellison 2008; Maiolino et al. 2008; Zahid et al. 2014; Sanders et al. 2015; Jones et al. 2020; Nakajima et al. 2023). Conversely, to date, only one study has focused primarily on RPS galaxies and attempted to investigate their MZR at $z \sim 0$ (Franchetto et al. 2020). Likewise, the relationship between the stellar-mass surface density, $\Sigma_\star$, and its local metallicity, known as the spatially resolved MZR, has been extensively explored over the past decade, primarily in galaxies not subject to ram-pressure stripping within the local Universe (e.g., Rosales-Ortega et al. 2012; Sánchez et al. 2013; Gao et al. 2018), yet investigations focusing on galaxies experiencing RPS remain notably absent. Due to its ability to accurately recreate the global metallicity and the metallicity profile over the galactocentric radius, the resolved MZR is seen by some authors as a more fundamental relationship than the global MZR (Barrera-Ballesteros et al. 2016).

The ongoing pursuit is to discern whether the impact of ram-pressure stripping varies over cosmic time. Specifically, the primary objective is to examine the interaction between the ISM and the ICM during ram-pressure stripping by analyzing their chemical compositions in clusters at $z \sim 0.35$. This paper exploits the MUSE guaranteed time observations (GTOs) from Richard et al. (2021) to trace the gas-phase metallicity within the disks and along the tails of a sample of RPS galaxies spanning a wide stellar-mass range. We focus on the global, spatially resolved, and radial distribution of the ionized gas metallicity of Abell 2744 and Abell 370 RPS members (Moretti et al. 2022) using MUSE data.

The paper is organized as follows: In Sect. 2 we present the galaxy sample obtained from the two closest clusters observed with the MUSE-GTO program. Section 3 outlines the tools and methods used in our analysis. In Sect. 4 we describe the methodologies employed to assess the gas-phase metallicity with indirect indicators. Section 5 presents our main results, which are discussed in Sect. 6. Finally, Sect. 7 summarizes the conclusions of this study.

2. Galaxy and cluster sample

In this paper we discuss Abell 370 and Abell 2744 (A370 and A2744, hereafter), the two most nearby clusters with the longest exposure time that have been observed within the MUSE-GTO program (Richard et al. 2021). The clusters are part of the Frontier Fields (Lotz et al. 2017). Additionally, A2744 is also part of the MAssive Clusters Survey (MACS; Ebeling et al. 2001) and has also been the target of multiple JWST campaigns (e.g., Treu et al. 2022; Bezanson et al. 2022). For both clusters a 2×2 MUSE mosaic exists, for a total exposure time of 20 h for A2744 and ∼19 h for A370 (Richard et al. 2021) with excellent seeing (∼0.61−0.66 arcsec).

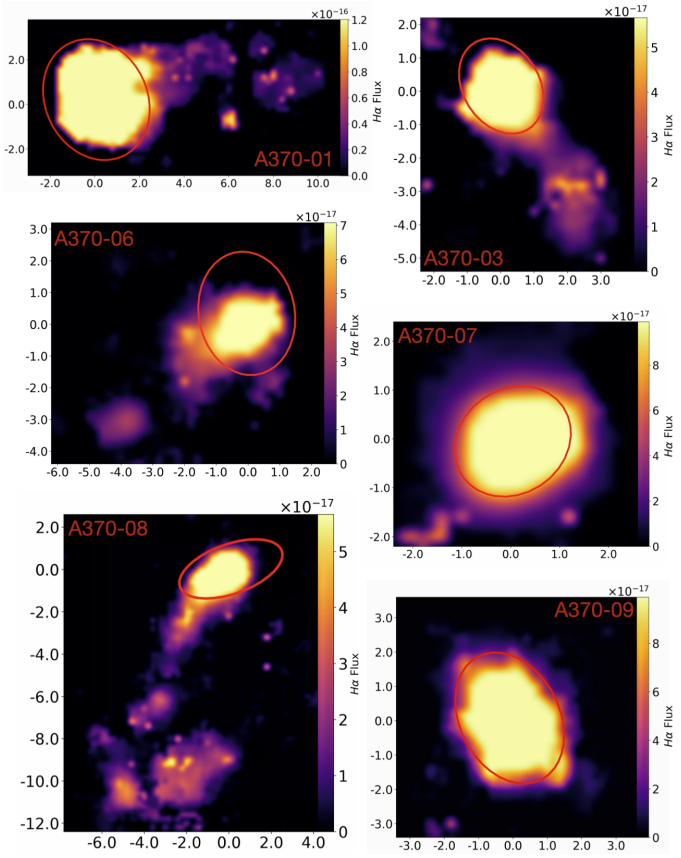

Fig. 1. Hα [erg cm^{-2} s^{-1} arcsec^{-2}] maps of RPS galaxies in the Abell 370 cluster obtained from MUSE data and smoothed via the bicubic interpolation method. The disk boundaries (Sect. 3.1) are illustrated with red ellipses. Both axes are in units of arcseconds.

We used the sample of galaxies classified as RPS by Moretti et al. (2022). The authors examined MUSE data cubes and *Hubble* Space Telescope (HST) red-green-blue images ($F435W + F606W + F814W$) to classify galaxies undergoing ram-pressure stripping. They were identified based on specific criteria: the presence of extraplanar, unilateral tails or debris with emission lines in the MUSE data cubes, and unilateral tails or debris visible in HST images, which were confirmed to be associated with the galaxy using MUSE redshift information. We have a total of 13 RPS galaxies at our disposal (Figs. 1 and 2) that are members of the two clusters. Most of them have a stellar mass exceeding $10^9\,M_\odot$, with only three exceptions. Notably, one galaxy, A370-02, is excluded from the analysis due to an insufficient number of spaxels with well-detected Hα emission lines. Additionally, in the case of A2744-01, nebular emission is exclusively present in the tail (Fig. 2) since the whole disk is in a post-starburst phase (lacking ionized gas; see Werle et al. 2022), our analysis exclusively focuses on the global properties of the tail in this galaxy.

A370 is a massive cluster at redshift 0.375 (Lah et al. 2009) with a reported mass of $8 \times 10^{14}\,M_\odot$ within 500 kpc and a velocity dispersion of ∼1300 km s^{-1} (Lagattuta et al. 2017). This cluster contains 153 spectroscopically confirmed members in the field covered by the MUSE mosaic. According to Moretti et al. (2022), after excluding A370-02 for the reasons mentioned earlier, the A370 cluster hosts 6 RPS galaxies (see Fig. 1) that

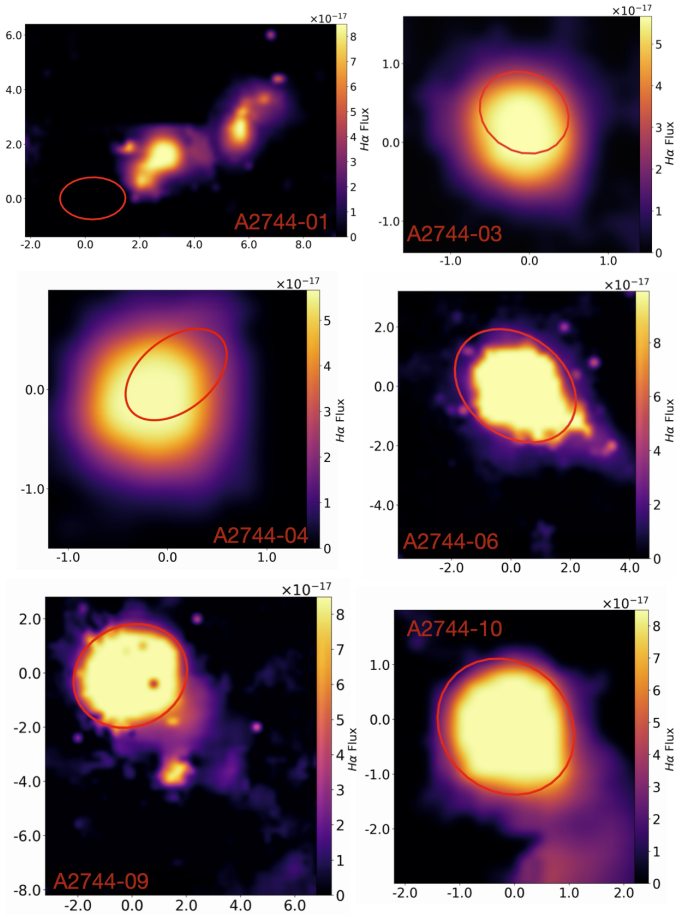

Fig. 2. Hα [erg cm^{-2} s^{-1} arcsec^{-2}] maps of RPS galaxies in the Abell 2744 cluster obtained from MUSE data and smoothed via the bicubic interpolation method. Both axes are in units of arcseconds, and disk boundaries are shown with red ellipses.

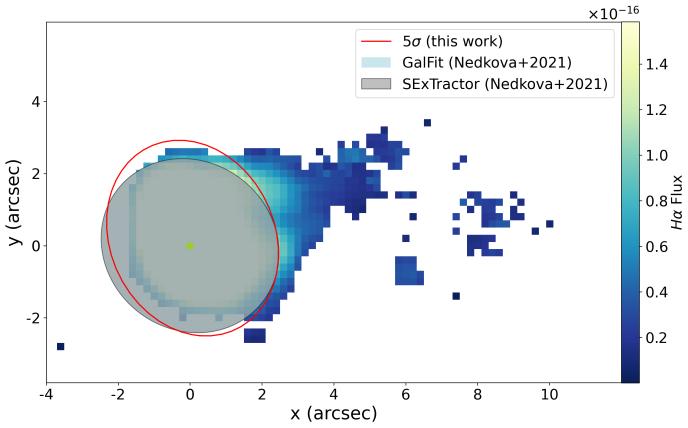

Fig. 3. A370-01 Hα [erg cm^{-2} s^{-1} arcsec^{-2}] map of star-forming regions (see Sect. 3.2) overlaid with disk masks. The red ellipse denotes the disk boundary. The SExTractor and GalFit disk position angles and ellipticities (which for this galaxy fully overlap), described in Sect. 3.1, are compatible with the 5σ contours. The size of the comparison ellipse was adjusted to be the closest to our 5σ contours for display purposes.

are located from the center out to $\sim 0.15\,R_{200}$ where R_{200} = 2.57 Mpc (Lah et al. 2009). Moreover, Bellhouse et al. (2022) demonstrated that although A370 is a merging cluster, there is no evidence to support the notion that the observed RPS galaxies are a consequence of the merger event. Rather, it is more probable that these galaxies are isolated infalling objects.

A2744 (also known as the Pandora cluster) is another intermediate redshift cluster at $z = 0.306$ (Owers et al. 2011). With a mass of $\sim 2 \times 10^{15}\,M_{\odot}$ (Jauzac et al. 2016), it contains 227 spectroscopically confirmed members in the field covered by the MUSE mosaic. In the study conducted by Owers et al. (2011), a comprehensive examination of the complex merging history of A2744 was carried out using X-ray and optical spectroscopy. They successfully identified two prominent substructures within the cluster, namely the northern core and the southern minor remnant core, along with a distinct region referred to as the central tidal debris. Remarkably, Bellhouse et al. (2022) demonstrated that the six RPS galaxies in A2744 are part of a cluster substructure and that their high-speed encounter with the dense X-ray gas associated with the southern minor remnant core is likely responsible for the stripping.

At the redshifts of these clusters, all main emission lines from $\lambda \sim 3500$ Å up to ~6800 Å rest frames are included in the MUSE spectra. Thus, we can derive dust correction and metallicity measurements with standard methods, as described below.

3. Data analysis

A number of spatially resolved characteristics and parameters, as well as integrated quantities of the gaseous and stellar components of our galaxy sample can be analyzed through the study of MUSE data. Stellar mass, stellar disk definition, gas kinematics, and ionization mechanism characteristics of the sample have been already presented in the previous study, Moretti et al. (2022). For our analysis, we needed to analyze disk and tail spectra and obtain the global and spatially resolved chemical composition of the galaxy sample. In this section we introduce the relevant tools and techniques.

3.1. Disk and tail configuration

We utilized the disk masks provided in Moretti et al. (2022) based on the MUSE g-band reconstructed image to define the galaxy boundary and be able to identify what is within the galaxy disk and what is the stripped matter. In Moretti et al. (2022), the centroid of the brightest central region in the MUSE g-band on the map was used to designate the galaxy's center. Then, by masking the galaxy itself and, if any, its companions, the local background sky's surface brightness was determined. The stellar isophote that corresponds to surface brightness 1.5, 3, and 5σ above the reported sky background level was then defined. Then, an ellipse was fitted to each isophotal level to define the galaxy boundary. The 5σ contours are superimposed onto Hα maps in Figs. 1 and 2.

We note that the definition of the parameters needed to distinguish between disk and tail might depend on the adopted band and algorithm. To assess the reliability of our measurements, we compared the ellipses used to define the disk masks to the ellipses obtained using the catalog of Nedkova et al. (2021), who measured structural parameters (e.g., position angle, inclination, and ellipticity) for *Hubble* Frontier Fields (HFFs; including A2744 and A370), supplementing the data release (v3.9) of HFF-DeepSpace (Shipley et al. 2018). We compared our results with their calculations of position angle and ellipticity (Fig. 3), which were obtained using two different algorithms, GALFIT and SExtractor, performed in the $F435W$ band, which closely corresponds to the g-band. In the majority of cases, our findings are in good agreement with the results obtained by

Nedkova et al. (2021). However, in three galaxies, we identified a discrepancy in the position angle that rendered it incompatible with the 5σ contour. Upon visual inspection, we have reached the conclusion that the 5σ contours align more closely with the information derived from the Hubble red-green-blue images. Hence, in the following, we use our 5σ contours to separate disks and tails in all galaxies.

3.2. Spectral analysis

The analysis of the MUSE data is extensively described in two key references, Poggianti et al. (2017) and Moretti et al. (2022). In a concise summary, MUSE spectra are corrected for the extinction caused by dust in our Galaxy. The stellar-only component of the spectrum in every spaxel of each galaxy is derived using the spectrophotometric fitting code SINOPSIS (Fritz et al. 2017) and is subtracted from each spaxel's spectrum to obtain the emission-only component. The stellar mass of each spaxel was obtained with SINOPSIS using the most recent update of the Bruzual & Charlot (2003) stellar population models (see Werle et al. 2019, for an outdated but still relevant description of the models) with a Chabrier (2003) initial mass function (IMF).

The gas kinematics, emission line fluxes, and associated errors are obtained using the software HIGHELF (Radovich et al., in prep.), which is based on the LMFIT[1] Python package, and fits Gaussian line profiles using either one or two components. These fluxes are then corrected for intrinsic dust extinction using the Cardelli et al. (1989) extinction curve assuming an intrinsic Balmer decrement of $H\alpha/H\beta = 2.86$.

Diagnostic line ratios are employed to distinguish star-forming regions (which are assumed to be collections of unresolved H II regions) from areas that are ionized by other mechanisms. Individual H II regions have typical sizes of tens to hundreds of parsecs and, hence, are not resolved with our spatial resolution (i.e., ∼3.2 kpc).

In the following, spaxels with signal-to-noise ratio $S/N \geq 2$ are characterized as star-forming using the [N II]λ6584/Hα versus [O III]λ5007/Hβ Baldwin, Phillips, and Terlevich (BPT) diagram (Baldwin et al. 1981) according to the demarcation lines proposed by both Kewley et al. (2001) and Kauffmann et al. (2003), as seen in Fig. 4 where the spaxels of all galaxies are collectively plotted. Those spaxels that lie between these two lines of demarcation are labeled as composite while active galactic nucleus (AGN) and Low-Ionization Nuclear Emission-line Region (LINER) regions are excluded from the rest of the analysis. For cases involving composite emissions, the observed line ratios might be influenced by additional ionization sources beyond star formation. These sources could potentially include AGN or LINER emissions (Filho et al. 2004), diffuse ionized gas (Vale Asari et al. 2019), shocks (Allen et al. 2008), or elevated turbulence resulting from factors such as mixing of ISM and ICM due to the ram-pressure stripping (Poggianti et al. 2019b). Consequently, spaxels classified as composite will be addressed individually in the subsequent spatially resolved analysis.

In addition to the spatially resolved analysis, in what follows we also consider global quantities, always separating disks and tails. To accomplish this, we integrated the spectra of the disk and tail of each galaxy separately. Stacking spectra improves metallicity measurements of weak spectral features in low-mass or low-surface-brightness galaxies (e.g., A2744-03 and A2744-04). It also allows for the statistical analysis of galaxy sample properties, particularly the global MZR. The results obtained by stacking are also more easily comparable to fiber or slit spectroscopic results (e.g., Maiolino et al. 2008; Mannucci et al. 2010; Bothwell et al. 2013; Curti et al. 2020) and future works at different redshifts. As an example, A370-01 disk's stacked emission-only spectrum is shown in Fig. 5. It contains the emission lines employed in the metallicity measurements. As an alternative method, we also used the median metallicity in the disk and the tail separately. In both methods, we only considered spaxels powered by star formation and composite emission.

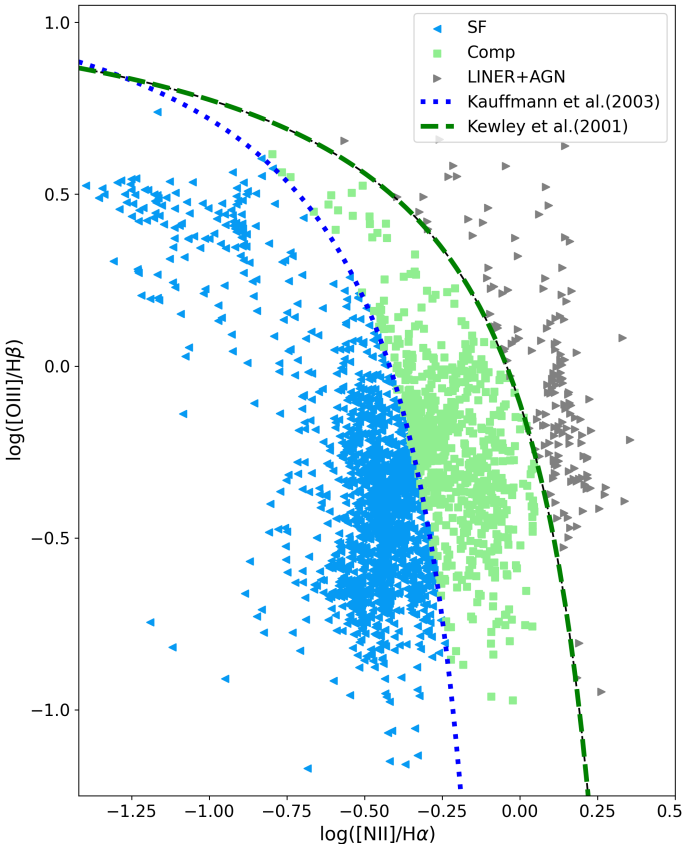

Fig. 4. BPT diagram of all spaxels in the galaxy sample. They are classified as star-forming (SF), composite (Comp), or AGNs and/or LINERs. The Kauffmann and Kewley demarcation lines in the [OIII]/Hα vs. [NII]/Hβ BPT diagram are indicated by the dotted and dashed lines, respectively.

4. Gas-phase metallicity measurements

In the realm of subsolar metallicities, the most precise method for determining the gas phase oxygen abundance is often achieved by ascertaining the electron temperature (also known as the direct method), as described by Pagel et al. (1992) and Izotov et al. (2006). This approach relies on the identification of faint auroral lines, which unfortunately remain largely undetectable within the average depth of observations conducted as part of the MUSE GTOs and similar spectroscopic surveys.

In this study, in the absence of direct temperature measurements, we effectively gauged the gas phase metallicity by using both a theoretical calibration through a photoionization model and an empirical calibration based on samples of H II regions with direct method abundances. These strong line diagnostics ratios were used as indirect indicators. Though it is well known that different indicators provide different metallicities on an absolute scale, we chose to use two independent methods,

[1] https://lmfit.github.io/lmfit-py/

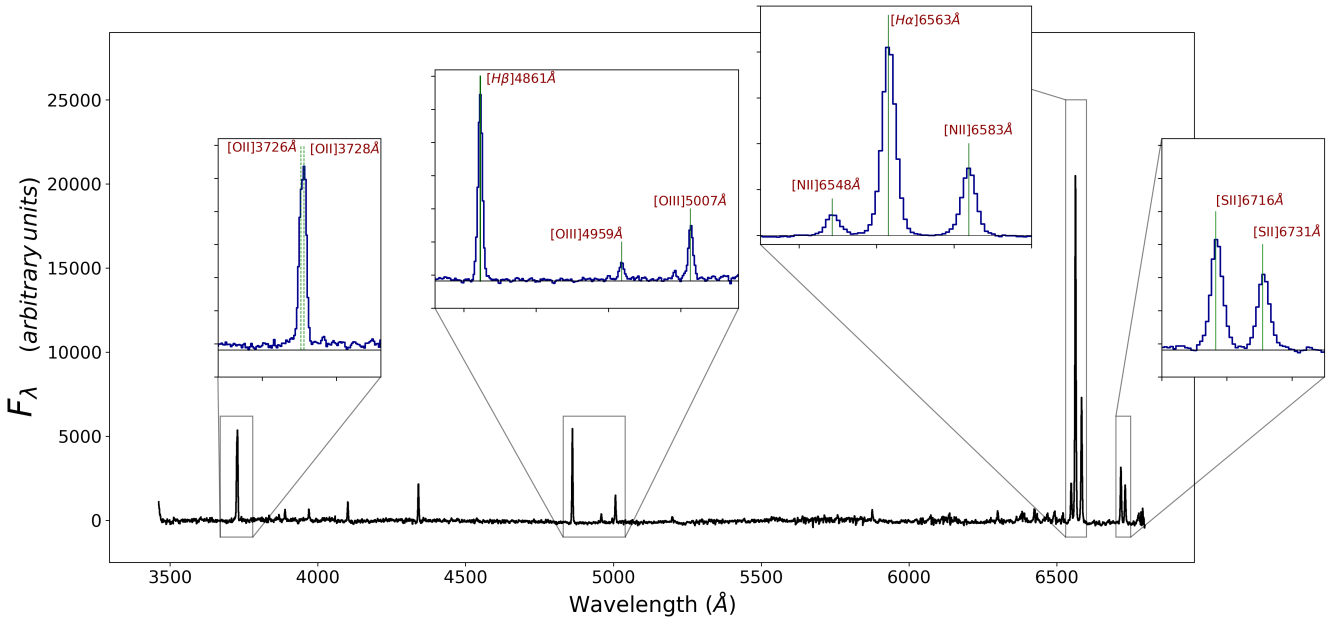

Fig. 5. Stacked rest-frame spectrum for the disk of A370-01. Note that the stellar contribution is subtracted from each spaxel's spectrum, prior to stacking. Only the region of interest for this paper is shown, from 3500 Å to 6800 Å. In this range we have the essential nebular lines of [OII], [SII], and [OIII] and H Balmer lines to measure the metallicity based on strong emission lines.

based on different assumptions, in order to verify the solidity of our qualitative conclusions.

4.1. Empirical metallicity measurement

The first calibration we used was introduced by Pettini & Pagel (2004, P04 hereafter). This is an empirical method, calibrated via electron temperature measurements, that determines the oxygen abundance in H II regions, particularly with an eye to their application to the analysis of star-forming galaxies at high redshifts. It is based on the O3N2 index, defined as $\mathrm{O3N2} \equiv \log[([\mathrm{O\,III}]\lambda5007/\mathrm{H}\beta)/([\mathrm{N\,II}]\lambda6584/\mathrm{H}\alpha)]$ according to the formula

$$12 + \log(\mathrm{O/H}) = 8.73 - 0.32 \times \mathrm{O3N2}. \quad (1)$$

Equation (1) is valid only for $\mathrm{O3N2} < 1.9$, corresponding to a minimum metallicity of ∼8.1. Spaxels with $\mathrm{O3N2} \geq 1.9$ must be excluded in our analysis, and represent <5% of our set of spaxels in each galaxy, except in A2744-04 in which they are ∼30% of usable spaxels. Notably, a probable systematic error in the super-solar metallicity regime affects the calibration (Stasińska 2002), which is empirical in nature and anchored to the abundances of 137 H II regions, six of which are determined through photoionization models and the rest by the direct method. Additionally, it should be emphasized that since [N II] and [O III] come from ions with a significant difference in ionization potential, changes in the ionization parameter, which are uncalibrated, consistently influence this diagnostic ratio (see, for instance, Blanc et al. 2015).

However, the O3N2 index offers the advantage of minimizing uncertainties resulting from flaws in flux calibration or extinction correction due to its reliance on line ratios that are close in wavelength and exhibit a monotonic change with metallicity. Consequently, it serves as a valuable calibration for measuring the metallicities of both the A370 and A2744 clusters. This calibration can also be applied to slightly more distant clusters observed with MUSE. Moreover, it is widely used at $z > 0$; hence, it is convenient to compare it with future works.

Using Monte Carlo simulations, the inferred P04 metallicity uncertainties are calculated by randomly perturbing (under the assumption of a Gaussian noise distribution) all recorded line fluxes by their measurement errors 1000 times. Thus, the metallicities are the median of these samples and the reported errors are their standard deviations. Nevertheless, we point out that since the systemic contributions are not taken into account, these values likely underestimate the actual uncertainty.

4.2. PYQZ

For a specific set of emission line fluxes, the PYQZ python library (Dopita et al. 2013; Vogt et al. 2015) concurrently delivers the gas metallicity and ionization parameter ($\log q$) values. In order to interpolate the $\log q$ and $12 + \log(\mathrm{O/H})$ values, a finite number of diagnostic line ratio grids was produced using the MAPPINGS code (Sutherland & Dopita 1993; Dopita et al. 2013). PYQZ creates N (i.e., $N = 400$ set as default) randomly chosen sets of emission-line fluxes, Gaussian distributed in accordance with the given flux errors, considering the available emission lines of each spectrum. The algorithm calculates the metallicity and the ionization parameter for each set, then performs a two-dimensional Gaussian kernel density estimate to create the probability density function (PDF) from the discrete distribution of the metallicity and ionization parameter values. To determine the metallicity uncertainty (Vogt et al. 2015), the algorithm propagates the PDF according to the flux measurement uncertainty and defines the metallicity errors as the 1σ contours of the PDF.

Here, we utilized the same modified version of PYQZ that was used by Franchetto et al. (2020). This version makes use of MAPPINGS IV to produce diagnostic line ratio grids and covers the range $7.39 \leq 12+\log(\mathrm{O/H}) \leq 9.39$, which works well even in the extremely high metallicity range, and the $6.5 \leq \log q \leq 8.5$ ionization parameter range. This PYQZ version covers a wider range of line ratios with respect to the latest official version (i.e., v0.8.4), thus allowing us to recover metallicities for a larger number of spaxels.

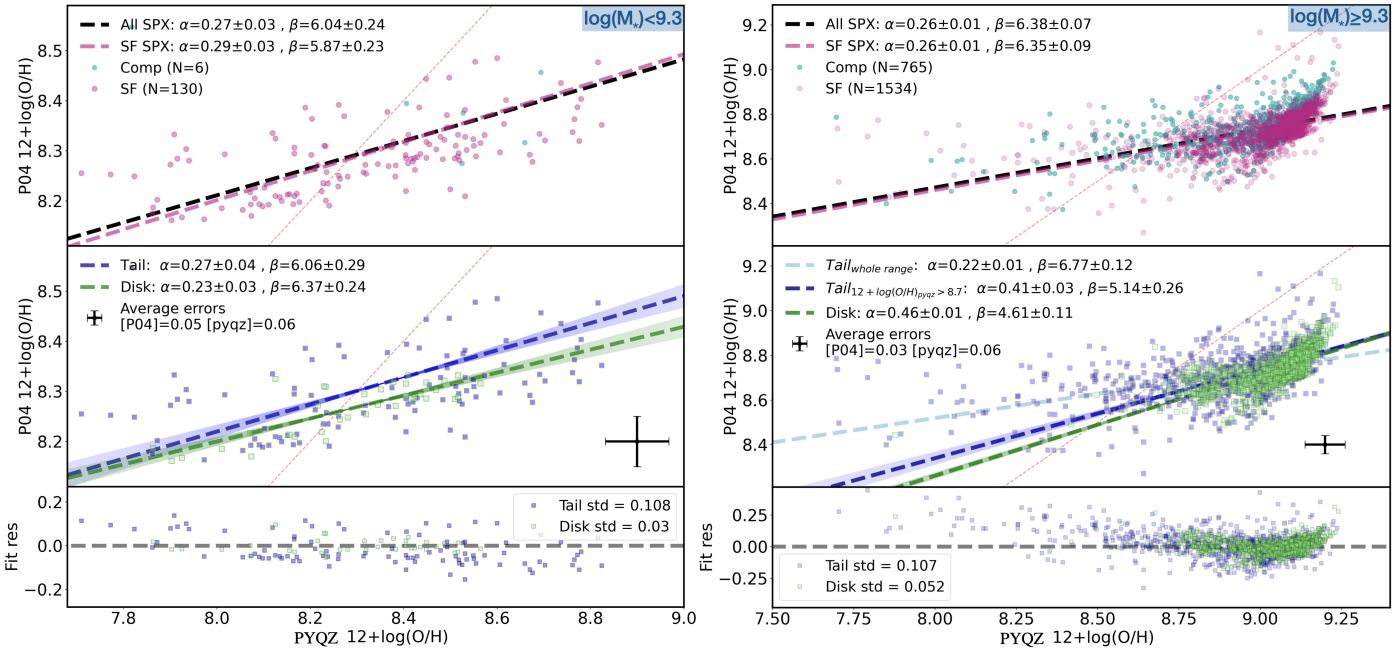

Fig. 6. Comparison of the metallicity measurements of all spaxels in all galaxies of our sample for the two different metallicity diagnostics. Right: high-mass galaxies ($\log(M_\star/M_\odot) \geq 9.3$). Left: low-mass galaxies ($\log(M_\star/M_\odot) < 9.3$). In both plots, the behavior of star-forming (SF) and composite (Comp) spaxels can be seen in the top panels. Their relationship is modeled via a linear approach and a least square fit, where $\mathrm{P04}_{12+\log(\mathrm{O/H})} = \alpha \times \mathrm{PYQZ}_{12+\log(\mathrm{O/H})} + \beta$. The dotted red line represents the one-to-one relation, while the dashed black and pink lines are the SF+Comp (all spaxels) and SF linear fits, respectively. Middle panels: disk (green) and tail (blue) spaxels are linearly modeled separately. The error bars are the metallicity uncertainties described in Sect. 4. Bottom panels: residuals from the overall fit (black line in top panel), with standard deviation (std) values shown.

We employed the [O III]4959, 5007 Å, [N II]6548, 6583 Å, and [S II]6716, 6730 Å doublets as inputs since they offer a solid distinction between $\log(q)$ and $12 + \log(\mathrm{O/H})$ and minimize the influence of the reddening correction uncertainty. We utilized the strongest line flux of each of the doublets [O III]4959, 5007 Å and [N II]6548, 6583 Å to reduce measurement uncertainty and calculate the amplitude of the weaker line using the ratio of the relative Einstein coefficient. As a result, the necessary emission line ratios are $(1.3 \times [\mathrm{O\,III}]\lambda5007)/([\mathrm{S\,II}]\lambda6716 + [\mathrm{S\,II}]\lambda6730)$ and $(1.3 \times [\mathrm{N\,II}]\lambda6584)/([\mathrm{S\,II}]\lambda6716 + [\mathrm{S\,II}]\lambda6730)$.

Furthermore, the PYQZ algorithm reports the uncertainty based on flux errors. It also suffers from not taking into account the systematic uncertainty, but Franchetto et al. (2020) offered an estimation of systematic error in relation to the PYQZ model grid uncertainty. In a nutshell, a model uncertainty of 0.1 dex results in a systematic error of 0.05 dex on the metallicity estimate for the highest metallicities ($12 + \log(\mathrm{O/H}) = 9.39$), while for the lowest metallicities ($12 + \log(\mathrm{O/H}) = 7.39$), the error can extend up to 0.3 dex. In our sample, the majority of oxygen abundances exceed 8.95. Consequently, considering the aforementioned systematic uncertainty associated with these abundances, we incorporated an additional 0.05 dex to the measured metallicity errors.

4.3. Method comparisons

Even when using the same diagnostic ratios, different calibrations can provide absolute metallicity estimates that vary by as much as 0.6 dex (Peña-Guerrero et al. 2012; López-Sánchez et al. 2012). Regardless of the absolute abundance scale problem (e.g., Kewley & Ellison 2008), which is beyond the scope of this work to resolve, Fig. 6 shows a strong correlation ($p > 0.6$) between the two metallicity calibrations, for the spaxels with both metallicity estimates and both for galaxies with mass below and above $M_\star = 10^{9.3}\,M_\odot$. Despite these strong correlations, minor discrepancies may arise in their behavior for specific scenarios (e.g., see Sects. 5.1 and 5.2.2).

We note that, as shown in the right plot's upper panel of Fig. 6, the correlation between the two metallicity indicators does not change when including or excluding composite spaxels. Moreover, the estimates given by the two indicators differ the most in the tails (middle and bottom panels in Fig. 6): in fact, the tail points are the most deviant from the linear fit with $\sigma \sim 0.1$ dex. More importantly, the tail and disk fit relations for high-mass galaxies have different slopes considering the whole range of metallicity (dashed light blue line), with negligible uncertainties as shown in Fig. 6. This discrepancy in the linear fit slopes is primarily attributed to the occurrence of low PYQZ metallicity estimations in certain tail spaxels, where the value of $12 + \log(\mathrm{O/H})_{\mathrm{PYQZ}}$ is less than 8.7. However, if we only consider tail spaxels with metallicities falling within the range covered by disk metallicities (i.e., $12 + \log(\mathrm{O/H})_{\mathrm{PYQZ}} > 8.7$), the slopes of the fits for disk and tail become more similar.

For this reason, and taking the additional factors mentioned earlier into account, in the following we exploit both indicators to assess whether results depend on the chosen indicator.

5. Results

We determined the metallicity value for each spaxel that meets the aforementioned BPT and signal-to-noise ratio ($S/N > 2$) criteria. In Fig. 7 we compare the metallicity map obtained by PYQZ (left panel) and P04 (right panel) of the galaxy A370-01, while Figs. 8 and 9 cover the rest of the sample. As these figures demonstrate, we can measure the gas metallicities also in regions outside of the stellar disk, in some cases only close to the disk

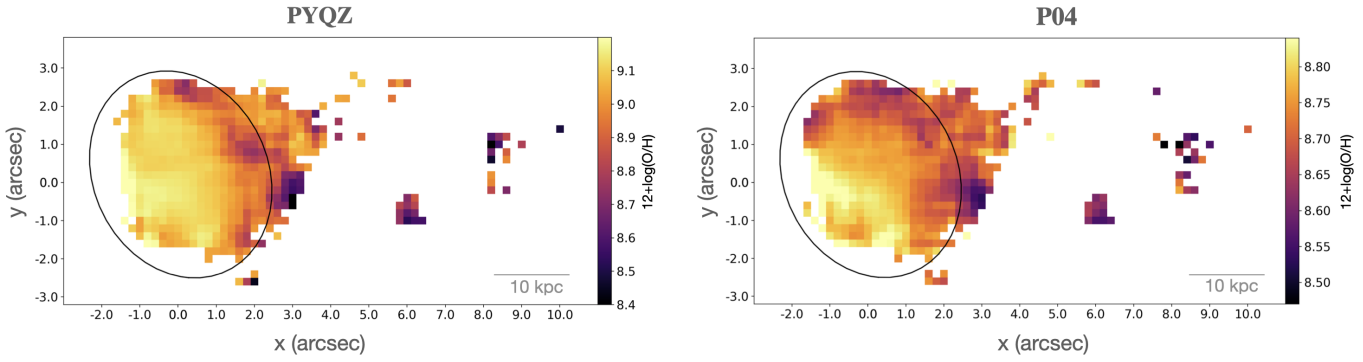

Fig. 7. A370-01 metallicity maps. The black ellipses identify the 5σ contour over the background, which we recognize as the disk boundary. The panels show the $12 + \log(O/H)$ maps calculated by PYQZ (left) and P04 (right). Since the two methods employ distinct emission lines to compute the metallicity (as mentioned in Sect. 4.3), they do not necessarily share the same usable spaxels. Additionally, as explained in Sect. 4, intrinsic variations in the estimated absolute values found using the two methods render it impractical to present maps with identical metallicity ranges as a colorbar.

outskirts and in other cases far from the disk, up to ~50 kpc away (e.g., A370-08).

5.1. Metallicity trend with projected distance

In order to investigate the behavior of oxygen abundances as we move farther from the central region of galaxies to their tails, we computed the metallicity as a function of angular distance. It is important to note that while a deprojection procedure for the disk could be accomplished using the disk axial ratio, the deprojection of the tail is impossible due to the unknown orientation. Our study primarily centers on comparing metallicities in both the disk and tail regions, and as such, we exclusively employed angular and projected distances in this study.

We present the metallicity gradient (projected) of all galaxies in our sample in Fig. 10, where we differentiate between star-forming and composite spaxels. The error bars represent the 1σ percentiles, while the median values reflect the median metallicity of each radial bin, considering both star-forming and composite regions. Below, we present a list of several observed features that can be noted upon initial examination.

i. The P04 and PYQZ metallicity trends qualitatively agree with one another, except in A370-03 where they differ only for the part of the tail that is closer to the disk, and in A2744-09 where the tail's trend is flat with respect to the disk using PYQZ, while the metallicity increases in the tail for P04.
ii. No large systematic difference in the metallicity gradient behaviors of star-forming and composite spaxels is seen since they mostly follow the same path, except for the fact that in a few of the disks, the most deviant points are composite (typically toward low metallicities). A separate fit for composite and star-forming spaxels is only possible for the tails of two galaxies, A370-03 and A370-09, where the best fit of star-forming and composite spaxels is consistent within the uncertainties. The composite deviant points in the disks (Fig. 11) are found either in the region of the disk where the tail begins (thus they might actually be already a part of the tail seen in projection onto the disk) or at the shock front caused by ram pressure, right at the leading edge of the disk. This is evident in cases like A370-01, A370-03, A2744-06, A2744-09, and A2744-10. A370-06, the only one with an AGN in the sample, and A370-08 stand out instead for having the whole disk dominated by composite spaxels.
iii. Metallicity trends in the disks are typically negative or flat with two positive exceptions, A370-06, and A2744-10. We note that A370-06, the one with the AGN, has a large number of AGN-powered spaxels along an extended ionization cone (see Moretti et al. 2022, and our Fig. 11), which are likely to affect our capability to assess the profile.
iv. In most cases, the tail metallicity declines with distance along the tail and is generally lower than in the corresponding disk, with three notable exceptions: A2744-04, A2744-09, and A2744-10. Moreover, the slope in the tail is often not the same as the slope in the disk (e.g., A370-03). This may be the result of projection effects since we were unable to establish the actual separation of tail spaxels from the galactic center.
v. Overall, the global metallicity gradient (disk + tail) is negative or almost flat (except for A2744-10 and P04 estimate of A2744-09, which have sharp positive slopes as already discussed above).

In addition, the ionization characteristics (composite vs. star-forming) of tails and disks are not necessarily coupled (see Fig. 11). In five galaxies, these properties agree, being both tail and disk dominated (>95%) either by star-forming (A370-07, A2744-03, AA2744-04, and A2744-10) or by composite emission (A370-06). However, in three other galaxies, the emission in the tail probably has a different origin from that in the disk (see the low-redshift studies Poggianti et al. 2019b; Tomičić et al. 2021). For instance, in A370-01 the tail is mostly composite while the disk is mostly star-forming. Also, there are cases such as A370-08 where the disk is dominated by composite emission, while in the tail numerous spaxels are found both in the composite and in the star-forming regime.

It is interesting to assess whether the observed trends depend on galaxy stellar mass. The two lowest-mass galaxies, A2744-03 and A2744-04 (on the order of $\log(M_\star/M_\odot) \sim 8$), have trends consistent with a flat metallicity gradient across disk and tail, although with a large uncertainty and a few points. Also, considering the proximity of the disk angular size of these galaxies to the observation's resolution limit, this might be simply a resolution effect. The only galaxy in which the tail metallicity appears to be consistently higher than in the disk (PYQZ), or at least to have a growing outward profile (P04), is A2744-10, with a mass $\log(M_\star/M_\odot) = 9.3$. As mentioned above, PYQZ and P04 results do not agree for A2744-09 and it is, therefore, hard to draw any conclusion for this galaxy. For all the other galaxies (all with

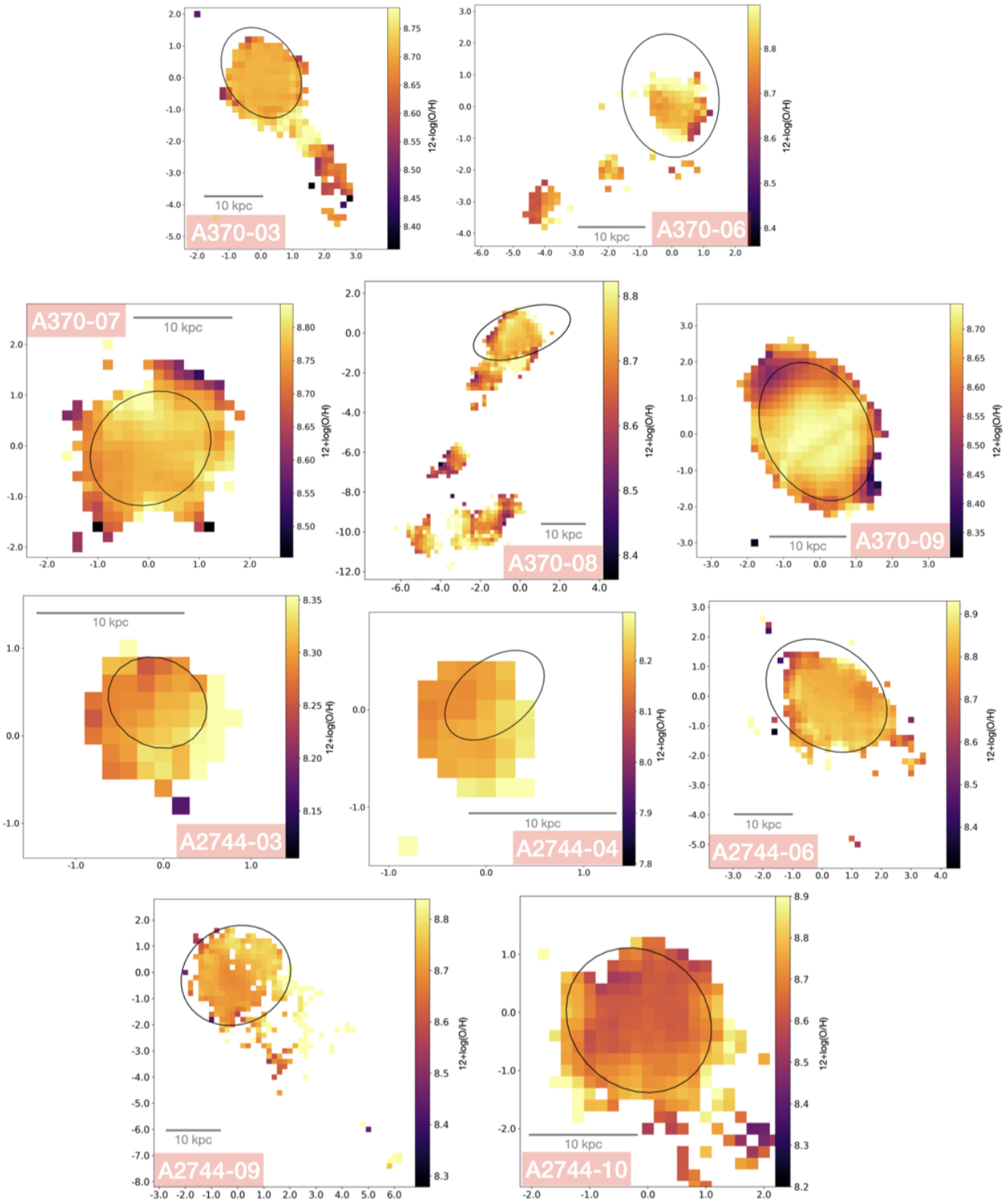

Fig. 8. P04 metallicity maps of ten RPS galaxies in the A370 and A2744 clusters. Each map's black outlined ellipse represents the 5σ contour, which is the boundary of the galaxy disk (see Sect. 3.1). Each plot also shows a scale corresponding to 10 kpc at the cluster redshift.

$\log(M_\star/M_\odot) \geq 9.7$) the tail reaches metallicities lower than anywhere in their disk.

Our findings are in line with the two existing studies to date at redshifts ∼0, as reported in Bellhouse et al. (2019) and Franchetto et al. (2021b). They examined the projected tail star-forming clumps of, respectively, 1 and 3 RPS galaxies with $\log(M_\star/M_\odot)$ equal to 10.55, 10.96, 11.21, and 11.50. These studies revealed a maximum metallicity difference of ∼0.5 dex between the nearest and farthest parts of the tails from the disk by using the same modified version of PYQZ used in this paper.

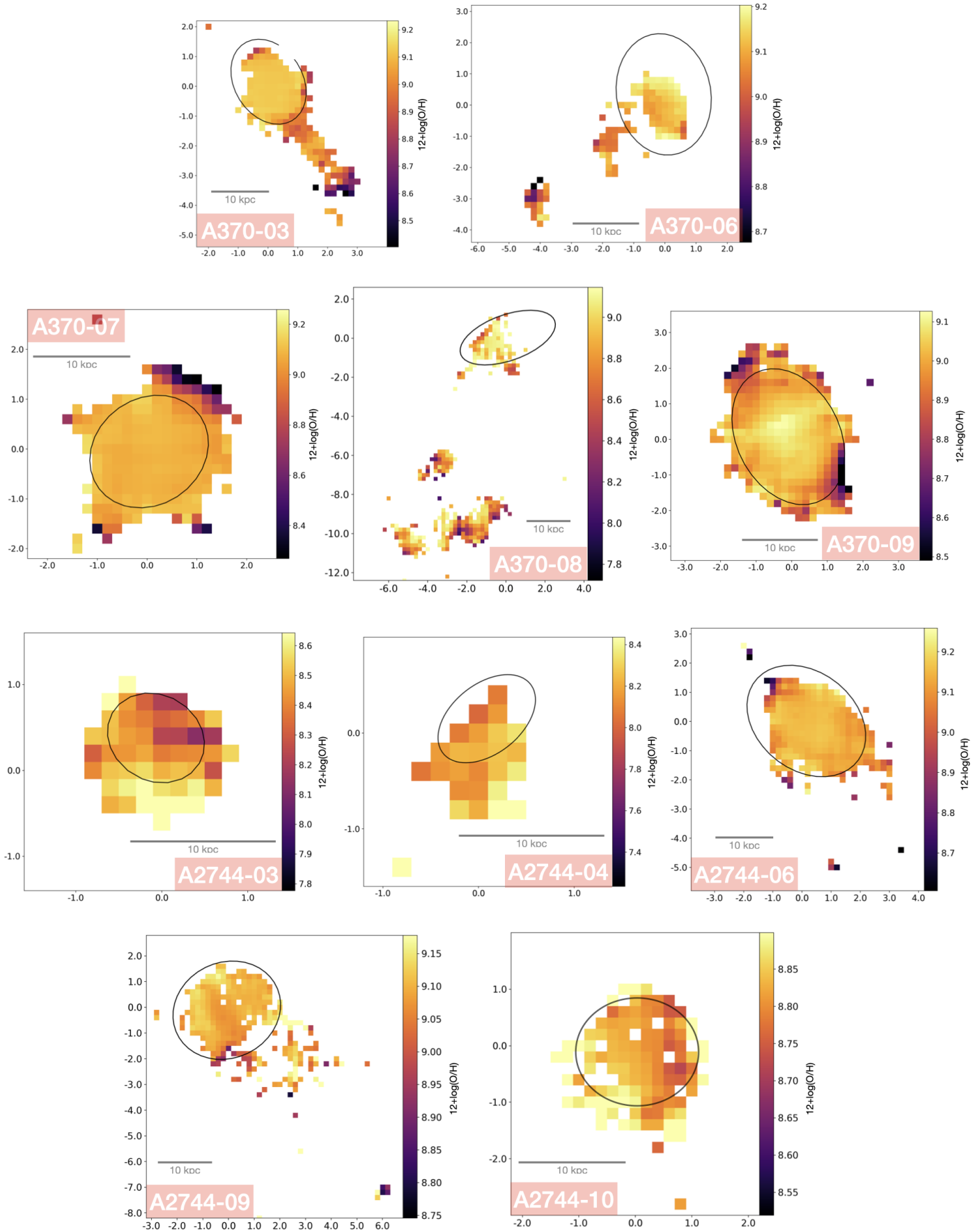

Fig. 9. PYQZ metallicity maps of ten RPS galaxies in the A370 and A2744 clusters. The 5σ contour, which is the boundary of the galaxy disk (see Sect. 3.1), is depicted as a black ellipse on each map. Additionally, a scale for 10 kpc at the cluster redshift is included for each plot.

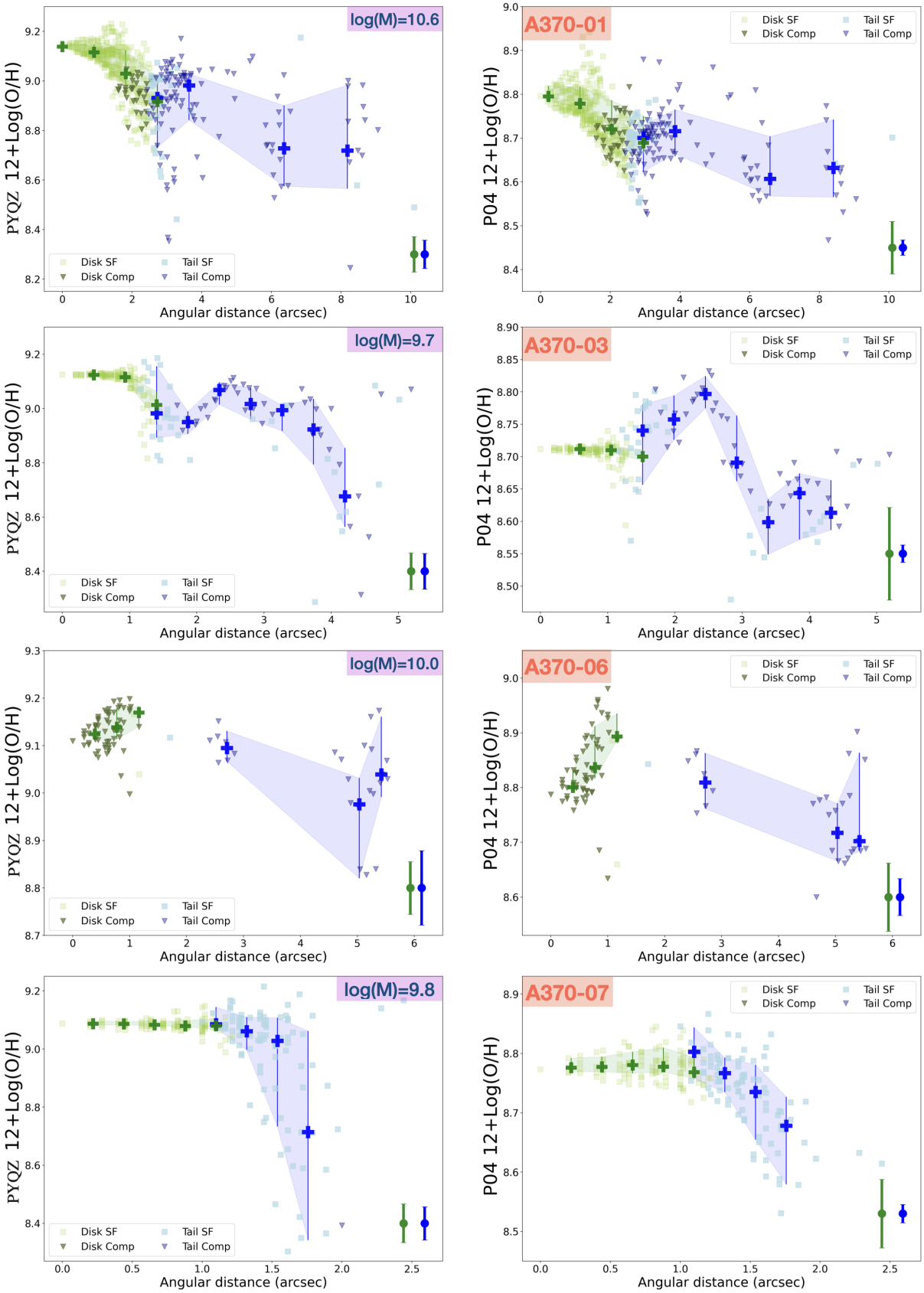

Fig. 10. Metallicity gradients computed using two different methods: PYQZ (left panel) and P04 (right panel). Disk and tail spaxels are color-coded in green and blue, respectively. Triangles represent composite spaxels (Comp) and squares star-forming spaxels (SF). The bold plus markers are median $12 + \log(\mathrm{O/H})$ values in each angular distance bin, and the associated error bars (and shades) represent the 1σ percentile. Also, the stellar mass of galaxies (M) is given in the left panels in solar mass units (continued in Fig. A.1).

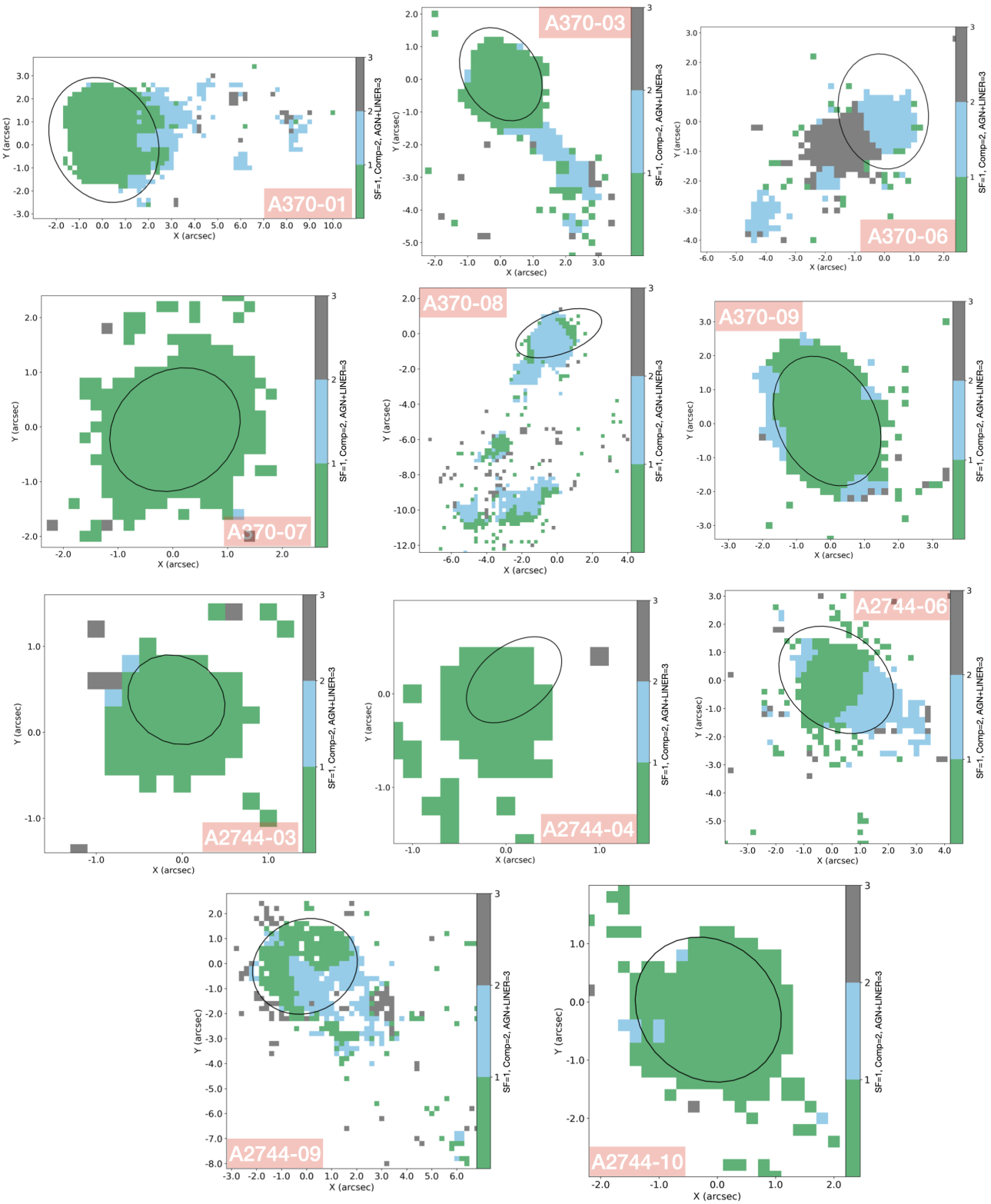

Fig. 11. BPT maps of 11 RPS galaxies in the A370 and A2744 clusters. Green spaxels are those dominated by star formation, blue ones are those classified as composites, and gray spaxels are those that lie either in the LINER or AGN regions.

It should be noted that the projected tail lengths observed in the sample of Bellhouse et al. (2019) and Franchetto et al. (2021b) are approximately 20−50 kpc.

In contrast, our own typical projected tail lengths are equal to or less than 20 kpc (with only one exception of ∼50 kpc), and at considerably higher redshifts. Also, due to the differences in the approach employed, with our analysis focusing on the metallicity of individual spaxels[2] while their work examined integrated spectra of star-forming clumps, a direct comparison with Franchetto et al. (2021b) is not feasible.

[2] The MUSE spatial resolution is not sufficient to identify individual star-forming clumps in $z \sim 0.3$ RPS galaxies.

5.2. Mass–metallicity relation

In this section we first discuss the spatially resolved MZR of each galaxy, distinguishing disk and tail spaxels. We then analyze the global MZR separately for disks and tails, to investigate whether the tail metallicity is correlated with galaxy mass as the disk metallicity is.

5.2.1. Spatially resolved mass–metallicity relation

Figure 12 presents the resolved MZR of the whole sample with a few exceptions. We note that SINOPSIS (see Sect. 3.2) cannot calculate the surface density of stellar mass for galaxies A2744-03 and A2744-04, since their spectra do not contain any information about the stellar continuum. Moreover, the surface density of stellar mass for A2744-10 is not yet available. This figure illustrates that in both metallicity diagnostics, P04 and PYQZ, the metallicity rises as we approach spaxels with higher stellar mass surface density, which is consistent with other findings on the resolved MZR (e.g., Rosales-Ortega et al. 2012; Yao et al. 2022). The tail of the galaxy does not reach the highest surface mass density reached in the disk and at any given mass density its median metallicity trend follows that of the disk, with values that are similar or slightly lower.

The resolved MZR of the disk is mostly flat or positive (only A370-01 and A370-09) and one case slightly negative (A2744-06). The stellar-mass surface densities of tail spaxels consistently populate the lower end of the density range observed in the disks, and they do not necessarily illustrate the same trend as the disks regardless of their parent galaxy stellar mass values (see Table 1). Moreover, the presence of spaxels in the tails with significantly lower metallicities than any disk spaxel of similar surface mass density is a noteworthy finding. This may indicate different enrichment processes in the tails compared to the disk, as previously mentioned.

5.2.2. Global mass–metallicity relation

The top panel of Fig. 13 shows the MZR (second-order polynomial fit) that we derive for the stacked spectra of individual galaxies. Disks and tails were investigated independently for two reasons. Firstly, it was crucial to ascertain whether tails and disks exhibit a consistent MZR. Secondly, we can investigate the variation in global metallicity between the disk and the tail concerning the parent galaxy's disk stellar mass and metallicity.

As seen in the top panel of Fig. 13, for PYQZ and P04, both disks and tails display a clear MZR. They notably follow a similar path with a positive slope (which is consistent with previous studies such as Maiolino et al. 2008; Sánchez et al. 2019; Nadolny et al. 2020), and a flattening at high masses, in each metallicity diagnostic. Although Franchetto et al. (2020), the sole analogous study available, utilized similar methodologies to those employed in this paper, a direct comparison of our results is unfeasible due to the use of distinct apertures. We contrasted our findings with the MZR proposed by Kewley & Ellison (2008), as shown in the top right panel of Fig. 13. Kewley & Ellison (2008) employed a sample of 27 730 star-forming galaxies at $z < 0.1$ obtained from the Sloan Digital Sky Survey (SDSS) DR4 catalog (thus fiber-integrated spectra) using the Salpeter (1955) IMF and the P04 metallicity calibration in their analysis. When we covert the Salpeter (1955) IMF to the Chabrier (2003) IMF, our findings are quite consistent with their relation within the reported uncertainty of 0.1 dex.

Furthermore, the global metallicity values of the disks and tails of individual galaxies exhibit a relative similarity, with the tail metallicities generally being slightly lower than those of their parent galaxy's disk, which is consistent with previous studies at low redshifts of individual galaxies by Fossati et al. (2016) and Gullieuszik et al. (2017) and the three galaxies studied by Franchetto et al. (2021a). Nevertheless, some exceptions exist, such as the galaxies A370-07 and A2744-03 in PYQZ and a galaxy, A2744-10, in the P04 diagnostic, where the tail global metallicities are up to ∼0.1 dex higher than their corresponding disk values. Stacking spaxel spectra can result in biased derived properties if highly luminous spaxels with higher metallicities dominate the combined spectrum, similar to biases caused by stacking spectra with different star formation histories. By analyzing the median metallicity, we are taking the distribution of metallicities within the sample into account, which are less susceptible to these biases.

In the bottom panel of Fig. 13 we present the MZR using the median metallicity value for the disk and tail regions, with the inclusion of only those spaxels that meet both the BPT diagram and S/N criteria (see Sect. 3.2). Also in this case, the global metallicities of the disks and tails within individual galaxies demonstrate a degree of similarity. However, it is noteworthy that the metallicities of the tails are generally slightly lower than those of the disks in their respective parent galaxies, with the exception of three cases, namely A2744-03 in the PYQZ, and A2744-09 and A2744-10 in the P04 metallicity diagnostic. Therefore, the overall trends remain consistent with those observed in Fig. 13's upper panel, where the MZR of the tail galaxies follows that of the disks, though with slightly but systematically lower metallicities at masses above $10^{9.3}\,M_{\odot}$.

Extraplanar tails of ionized-stripped gas, extending up to several tens of kiloparsecs beyond the stellar disk, are often observed in RPS galaxies in low-redshift clusters. Recent studies have also identified similar tails at high redshifts, and we here present the first analysis of the chemical composition of such tails beyond the local Universe. At first, we examined the resolved distribution of ionized gas metallicity of RPS galaxies in the Abell 2744 ($z = 0.308$) and Abell 370 ($z = 0.375$) clusters, the two most nearby clusters with the longest exposure time observed as part of the MUSE-GTO program. We investigated spatially resolved and global metallicities in galactic disks and stripped tails, utilizing both a theoretical calibration through a photoionization model and an empirical calibration. The metallicity gradients and the spatially resolved MZRs indicate that the metallicity in the tails reaches up to ∼0.6 dex lower values than anywhere in the parent disks, with a few exceptions. Both disks and tails follow a global MZR, though the tail metallicity is systematically lower than the one of the corresponding disk by up to ∼0.2 dex. These findings demonstrate that additional processes are at play in the tails, and are consistent with a scenario of progressive dilution of metallicity along the tails due to the mixing of ICM and interstellar gas, in accord with previous low-z results. Additionally, we examined all RPS in the other 10 clusters, $0.3 < z < 0.55$, observed via the MUSE-GTO program alongside a control sample consisting of field and cluster galaxies. Through an examination of their disk chemical compositions, we unveiled unique characteristics exhibited by RPS galaxies, providing valuable insights into the interaction between the ISM and the ICM during ram-pressure stripping and the environmental impact on galaxy evolution at intermediate redshifts.

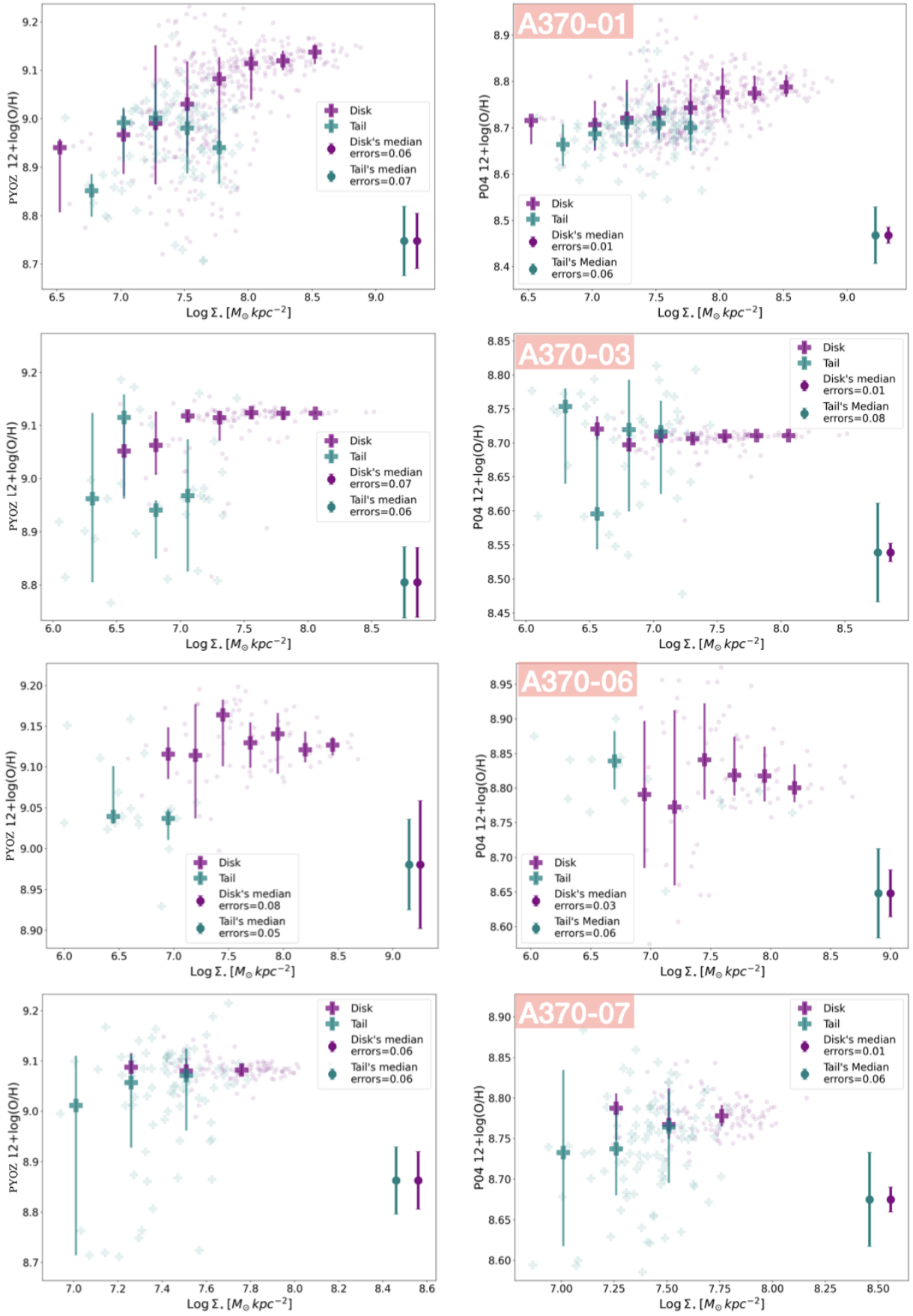

Fig. 12. Resolved MZR of eight RPS galaxies in A370 and A2744. The disk and tail spaxels with their accompanying metallicity uncertainty are color-coded in faded purple and teal, respectively. The bold plus markers provide the median metallicity values in stellar-mass surface density bins with 0.25 dex widths. The median value error bars represent the 1σ percentile deviation from the median value in each bin (continued in Fig. A.3).

Table 1. P04 and PYQZ stacked and median metallicity values of individual galaxies.

			P04				PYQZ			
ID	$\log(M_\star)$	z	Stacked disk	Stacked tail	Median disk	Median tail	Stacked disk	Stacked tail	Median disk	Median tail
A370-01	10.6	0.3738	8.76 ± 0.001	8.71 ± 0.01	8.75 ± 0.03	8.69 ± 0.07	9.13 ± 0.07	9.04 ± 0.07	9.08 ± 0.06	8.93 ± 0.07
A370-03	9.7	0.3580	8.71 ± 0.003	8.72 ± 0.03	8.71 ± 0.02	8.69 ± 0.08	9.17 ± 0.08	9.11 ± 0.06	9.12 ± 0.07	8.98 ± 0.06
A370-06	10.0	0.3593	8.83 ± 0.02	8.80 ± 0.03	8.82 ± 0.04	8.78 ± 0.07	9.23 ± 0.10	9.15 ± 0.09	9.13 ± 0.09	–
A370-07	9.8	0.3803	8.78 ± 0.01	8.76 ± 0.02	8.78 ± 0.02	8.74 ± 0.06	9.09 ± 0.05	9.16 ± 0.06	9.08 ± 0.06	9.05 ± 0.06
A370-08	10.1	0.3872	8.76 ± 0.01	8.76 ± 0.02	8.75 ± 0.04	8.73 ± 0.08	–	–	9.06 ± 0.08	8.82 ± 0.06
A370-09	10.0	0.3454	8.71 ± 0.01	8.63 ± 0.02	8.69 ± 0.01	8.61 ± 0.07	9.06 ± 0.06	8.98 ± 0.05	9.03 ± 0.05	8.97 ± 0.06
A2744-01	8.5	0.2919	–	8.18 ± 0.03	–	8.31 ± 0.06	–	7.73 ± 0.10	–	8.37 ± 0.07
A2744-03	7.9	0.3026	8.31 ± 0.02	8.28 ± 0.05	8.30 ± 0.04	8.32 ± 0.06	8.46 ± 0.06	8.50 ± 0.06	8.41 ± 0.07	8.54 ± 0.05
A2744-04	8.0	0.2941	8.22 ± 0.03	8.20 ± 0.05	8.21 ± 0.04	8.20 ± 0.05	8.23 ± 0.08	7.69 ± 0.05	8.16 ± 0.07	8.18 ± 0.06
A2744-06	10.0	0.2933	8.80 ± 0.002	8.80 ± 0.05	8.82 ± 0.03	8.78 ± 0.07	9.20 ± 0.08	9.14 ± 0.06	9.15 ± 0.07	9.08 ± 0.05
A2744-09	10.6	0.2956	8.67 ± 0.001	8.60 ± 0.05	8.73 ± 0.04	8.82 ± 0.08	9.17 ± 0.11	–	9.10 ± 0.06	9.08 ± 0.05
A2744-10	9.3	0.2958	8.59 ± 0.001	8.69 ± 0.03	8.65 ± 0.03	8.75 ± 0.08	8.87 ± 0.10	8.81 ± 0.05	8.80 ± 0.05	–

Notes. The $M_\star$ values are in units of $M_\odot$. The uncertainties in the stacked spectra metallicity are determined according to the method outlined in Sect. 4, and the median metallicity errors are obtained by averaging the uncertainties of spaxels within disks and tails.

6. Discussion

At low redshifts, the gas metallicity of Hα-bright clumps in RPS tails progressively decreases with increasing distance from the galaxy disk. This result was found for four strongly RPS galaxies at $z \sim 0.05$ by Franchetto et al. (2021b) and Bellhouse et al. (2019). The metallicity gradients of high-mass RPS galaxies ($\log(M_\star/M_\odot) > 9.3$) in clusters at $z = 0.3$–0.4 presented in this work generally show qualitatively similar trends to those observed in low-redshift RPS massive galaxies (with one notable exception, A2744-09).

Franchetto et al. (2021b) presented three possible scenarios to explain the observed lower metallicity values in the tails of their three galaxies. The first scenario proposes that the progressively lower-metallicity gas observed further out in the tail might have been removed from the disk at large galactocentric radii, where typically is less metal-enriched, following the inside-out formation of disk galaxies. The authors dismissed this scenario as unrealistic because the stripped tails maintain their radius or get wider with distance from the disk; therefore, the observed ionized gas cannot be stripped from well beyond the stellar disk. The same reasoning also applies to our sample, ruling out the first scenario.

The second scenario suggests that the observed metallicity values in the tails are due to the contamination of an additional ionization source that might alter the observed line ratios and metallicity measurements. Scenario two was also disregarded by Franchetto et al. (2021b) because their analysis was conducted ensuring that only star-forming clumps were considered, based on the BPT diagram, though the authors noted that they could not exclude the possibility that exotic processes might produce artifacts in the metallicity measurement. Regarding the second scenario for our sample, we note that emission that is classified as "composite" from the BPT diagram might be affected by ionization sources other than star formation. However, the second scenario is unlikely also in our case, because a strong declining trend is observed in the tails also when considering only star-forming spaxels (e.g., A370-03, A370-08, and others). It is worth noting that in their study, Franchetto et al. (2021b) incorporated an additional [OI]–[OIII] Kewley et al. (2001) BPT demarcation line to differentiate star-forming regions. We tried applying these criteria also to our entire sample, finding that 87% of the mutually selected regions are considered star-forming based on our [OIII]–[NII] Kewley et al. (2001) analysis. This indicates that our results are fully compatible with the findings of Franchetto et al. (2021b), even when considering additional line ratios. Furthermore, in the [SII]–[OIII] BPT diagram (Kewley et al. 2001), renowned for its sensitivity to detecting shocks, it is noteworthy that over 93% of spaxels identified as star-forming or composite in this work reside below the Kewley et al. (2001) [SII]–[OIII] BPT demarcation line. As an additional examination, we adopted the methodology proposed by D'Agostino et al. (2019) to investigate footage of shocks in the correlation between [OI]λ6300/Hα, [SII]λ6716,6730/Hα, [NII]λ6583/Hα, and velocity dispersion. Notably, our analysis revealed the absence of a robust correlation, thereby dismissing shock processes as a substantial source of contamination in our sample.

The third scenario postulated by Franchetto et al. (2021b) concludes that the low metallicity values in the tails are due to the mixing of the stripped ISM with the metal-poor ICM. Considering this the most plausible explanation, the authors provided a rough estimation of the mixing impact on the final gas metallicity. Interpreting our trends with the same arguments above, we conclude that the most likely explanation for our results is that the mixing of ICM and stripped ISM is efficient also at these redshifts and appears to be the underlying cause of the observed metallicity trends in the tails of distant cluster galaxies. Moreover, in recent X-ray investigations (Poggianti et al. 2019a; Campitiello et al. 2021; Bartolini et al. 2022), it has been suggested that the pronounced X-ray emission observed in the tail is predominantly attributed to the ISM–ICM mixing, supporting the scenario where the stripped ISM undergoes heating due to its interaction with the ICM. These findings are also supported by numerical simulations studies (e.g., Tonnesen et al. 2011; Tonnesen & Bryan 2012), which have reported a wide distribution of electron density and temperature across both the tail and the disk. Therefore, in response to the heating observed in X-ray studies, we utilized realistic electron temperature values for HII regions to model the oxygen abundances in both disks and tails. Our results not only corroborate this heating phenomenon but also reinforce the concept of elevated temperatures within the tail. Specifically, our results demonstrate consistency with the

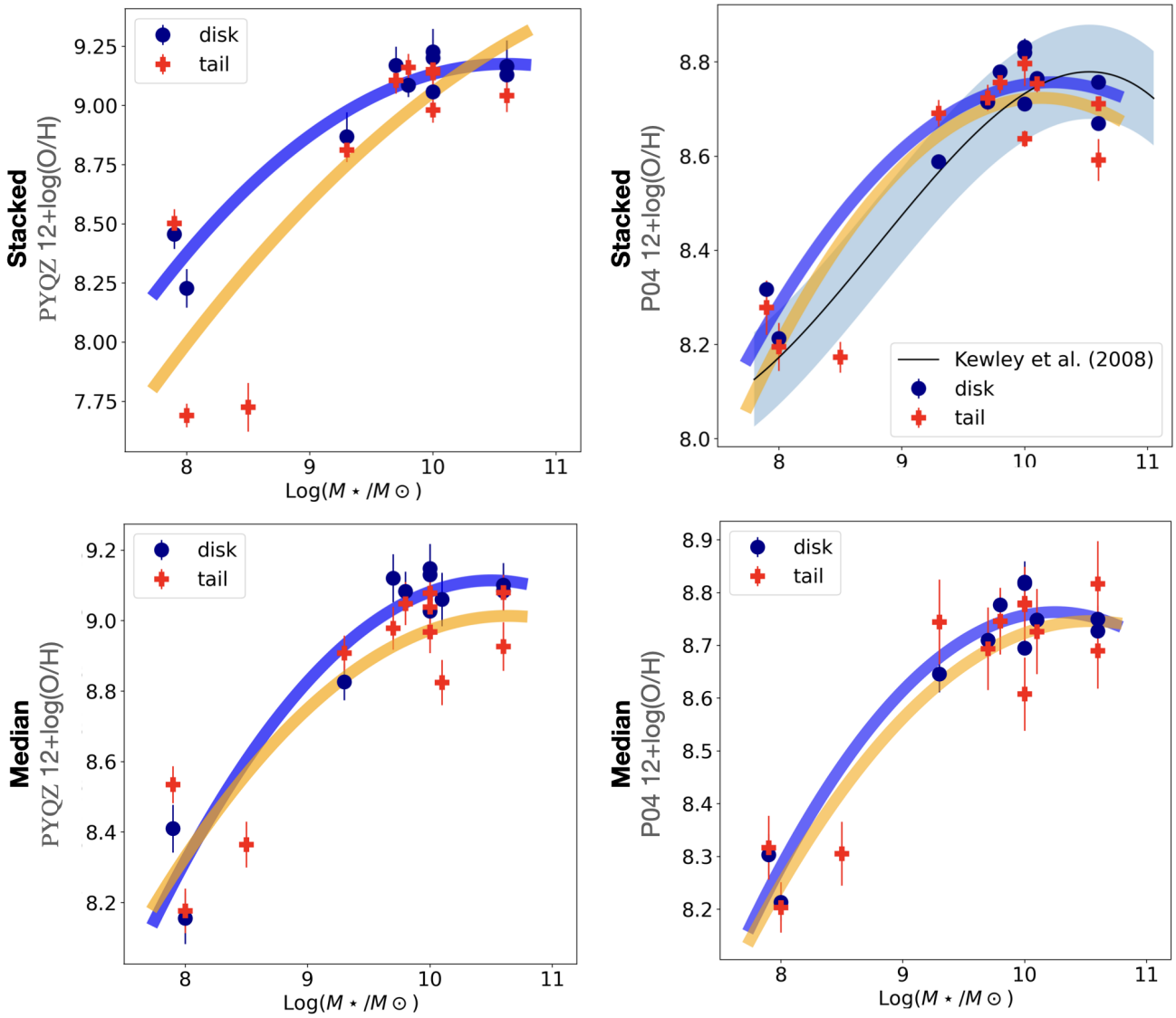

Fig. 13. Measured global MZR of all galaxies in the sample from stacked spectra (top plots) and assigning global median metallicity values (bottom plots) of tails (red with orange fit) and disks (dark blue with blue fit) via a second-order polynomial fit. The left and right panels show the PYQZ and P04 MZR, respectively. In both panels, error bars represent the metallicity uncertainty as discussed before. Additionally, due to the lack of usable individual spaxels in A2744-01, there is no median metallicity value available for the disk of this galaxy. In the right panels the metallicity of A2744-10's tail (i.e., the one with a steep positive gradient in Fig. 10) is higher than the disk's by 0.11 dex, which is exceptional. The solid black line represents the Kewley & Ellison (2008) MZR fit, with the 0.1 dex uncertainty illustrated with the blue shaded area.

trends highlighted in Sect. 5, where similar findings emerge only when tail temperatures surpass those of their respective disks.

Regarding the ISM–ICM mixing scenario, further detailed studies might be helpful to shed light on ICM enrichment and its current metallicity in different regions since the enrichment of the tail involves a multitude of processes beyond ISM–ICM mixing. It is imperative to delve into a deeper understanding of various aspects, including the stripping stages of a galaxy, star formation within the tail, density and temperature distribution, and a comprehensive knowledge of ICM characteristics across different regions within a cluster.

7. Summary and conclusion

In this paper we have studied the chemical evolution of galaxies at intermediate redshifts that are undergoing ram-pressure stripping, investigating how the intrinsic properties of galaxies, such as their stellar mass, influence the metallicity of the ISM and stripped-out gas in these entities. In order to do that, we used the data collected by MUSE via the MUSE-GTO program and the prior detections of RPS candidates in the Abell 370 and Abell 2744 clusters provided by Moretti et al. (2022).

We focused on the gas content of 12 RPS galaxies whose metallicities were studied via theoretical and empirical methods. Two methods were adopted: a photoionization model, PYQZ, and an empirical calibration, P04. We explored the metallicity gradient along the projected disk and tail of individual galaxies, considering both star-forming and composite regions. Moreover, for galaxies that contain meaningful stellar-continuum information, we studied the spatially resolved MZR of the disks and tails separately. We also investigated the global metallicity distribution using two approaches as detailed in Sect. 5.2.2. The main results of this study are as follows.

– P04 and PYQZ generally agree on metallicity trends, except in a very few cases. Moreover, the results from the integrated

spectra and median metallicity values are qualitatively consistent, regardless of whether we used the P04 or PYQZ diagnostic.

– In principle, composite emission is prone to inaccuracy due to other ionization sources, such as AGNs, LINERs, shocks, or high turbulence. This issue is even more complex in RPS tails, where composite emission may arise from ISM–ICM mixing. The presence of numerous composite spaxels in some of the disks suggests either the effect of mixing on the disk or the misidentification of extraplanar spaxels as a disk. The metallicity gradients of star-forming and composite spaxels show little systematic difference, as they usually follow a similar path. Although composite spaxels can be the most deviant in some disks, especially at low metallicities, they do not significantly alter the negative profiles or the comparison of metallicity measurement methods.

– Most disk profiles are negative or flat. Tail profiles are usually negative, with varying slopes from the disk, likely due to projection effects. Also, in most cases, the majority of the tail metallicities are lower than those of the disks. As a result, the overall gradient (disk + tail) is negative or nearly flat, with two exceptions. The present finding is consistent with the only existing study of RPS galaxies, which are at a low redshifts, Franchetto et al. (2021b).

– The vast majority of the studied galaxies, which have a $\log(M_\star/M_\odot)$ greater than or equal to 9.7, show tails with metallicities lower than those anywhere in their disks. Instead, the profiles across the disk and tail of the two lowest-mass galaxies, approximately $\log(M_\star/M_\odot) \sim 8$ (with a high degree of uncertainty and only a few available points), show a trend consistent with being flat.

– The flat metallicity gradients of low-stellar-mass galaxies ($\log M < 10^9\, M_\odot$) may be consistent with the mixing scenario too, considering that in low-mass galaxies the (low) metallicity of the ISM can approach the value of the ICM metallicity. However, given the closeness of the disk angular size of these galaxies to the resolution limit of our observations, it is hard to assess the meaning of this finding.

– The spatially resolved relation between the metallicity and the surface stellar-mass density (the resolved MZR) of the disks is generally flat or positive, with only one galaxy showing a slight negative trend. Tail spaxels, on the other hand, consistently display lower surface mass densities compared to their disk counterparts, regardless of the parent galaxy's stellar mass values (Table 1). The presence of tail spaxels with substantially lower metallicities than any disk spaxel with a similar surface mass density is evident from our data. This observation further reinforces the idea that different formation or enrichment processes are at work in the tails compared to the disk.

– The global MZRs of tails and disks determined using both the PYQZ and P04 calibrations exhibit the same trends. They share a similar positive slope, as observed in previous studies. Additionally, the global metallicity values of the tails and disks within each galaxy are relatively alike, but tail metallicities are generally slightly lower than those of the disk (except for a few galaxies in which the trend is inverted), which is consistent with previous studies by Franchetto et al. (2020, 2021b) and Gullieuszik et al. (2017). The most likely explanation for such trends is the mixing of the enriched gas stripped from massive galaxies with the lower-metallicity ICM.

In conclusion, the observations presented in this study suggest that the metallicity distribution in the tails of galaxies is shaped both by the metallicity of the parent galaxy and by the mixing with the metal-poor ICM as a result of ram-pressure stripping. This finding is supported by the observed steep negative profiles in massive (metal-rich) galaxies and the lower global metallicity values of tails compared to their parent disks.

Acknowledgements. We thank the referee for helpful comments that improved the paper. This project, funded by the European Research Council (ERC) under the European Union's Horizon 2020 research and innovation programme (grant agreement No. 833824), is based on observations gathered at the European Organization for Astronomical Research in the Southern Hemisphere, under the ESO programme 196.B-0578. This work used products from HFF-DeepSpace, funded by the National Science Foundation and Space Telescope Science Institute (operated by the Association of Universities for Research in Astronomy, Inc., under NASA contract NAS5-26555).

References

Allen, M. G., Groves, B. A., Dopita, M. A., Sutherland, R. S., & Kewley, L. J. 2008, ApJS, 178, 20
Bacchini, C., Mingozzi, M., Poggianti, B. M., et al. 2023, ApJ, 950, 24
Baldwin, J. A., Phillips, M. M., & Terlevich, R. 1981, PASP, 93, 5
Barrera-Ballesteros, J. K., Heckman, T. M., Zhu, G. B., et al. 2016, MNRAS, 463, 2513
Bartolini, C., Ignesti, A., Gitti, M., et al. 2022, ApJ, 936, 74
Bellhouse, C., Jaffé, Y. L., McGee, S. L., et al. 2019, MNRAS, 485, 1157
Bellhouse, C., Poggianti, B., Moretti, A., et al. 2022, ApJ, 937, 18
Bezanson, R., Labbe, I., Whitaker, K. E., et al. 2022, ApJ, submitted [arXiv:2212.04026]
Blanc, G. A., Kewley, L., Vogt, F. P. A., & Dopita, M. A. 2015, ApJ, 798, 99
Boselli, A., & Gavazzi, G. 2006, PASP, 118, 517
Boselli, A., Voyer, E., Boissier, S., et al. 2014, A&A, 570, A69
Bothwell, M. S., Maiolino, R., Kennicutt, R., et al. 2013, MNRAS, 433, 1425
Bruzual, G., & Charlot, S. 2003, MNRAS, 344, 1000
Campitiello, M. G., Ignesti, A., Gitti, M., et al. 2021, ApJ, 911, 144
Cardelli, J. A., Clayton, G. C., & Mathis, J. S. 1989, ApJ, 345, 245
Chabrier, G. 2003, PASP, 115, 763
Chung, A., van Gorkom, J. H., Kenney, J. D. P., Crowl, H., & Vollmer, B. 2009, AJ, 138, 1741
Curti, M., Mannucci, F., Cresci, G., & Maiolino, R. 2020, MNRAS, 491, 944
D'Agostino, J. J., Kewley, L. J., Groves, B. A., et al. 2019, MNRAS, 485, L38
Dopita, M. A., Sutherland, R. S., Nicholls, D. C., Kewley, L. J., & Vogt, F. P. A. 2013, ApJS, 208, 10
Ebeling, H., Edge, A. C., & Henry, J. P. 2001, ApJ, 553, 668
Filho, M. E., Fraternali, F., Markoff, S., et al. 2004, A&A, 418, 429
Fossati, M., Fumagalli, M., Boselli, A., et al. 2016, MNRAS, 455, 2028
Franchetto, A., Vulcani, B., Poggianti, B. M., et al. 2020, ApJ, 895, 106
Franchetto, A., Mingozzi, M., Poggianti, B. M., et al. 2021a, ApJ, 923, 28
Franchetto, A., Tonnesen, S., Poggianti, B. M., et al. 2021b, ApJ, 922, L6
Fritz, J., Moretti, A., Gullieuszik, M., et al. 2017, ApJ, 848, 132
Fumagalli, M., Fossati, M., Hau, G. K. T., et al. 2014, MNRAS, 445, 4335
Gao, Y., Wang, E., Kong, X., et al. 2018, ApJ, 868, 89
Gullieuszik, M., Poggianti, B. M., Moretti, A., et al. 2017, ApJ, 846, 27
Gullieuszik, M., Poggianti, B. M., McGee, S. L., et al. 2020, ApJ, 899, 13
Gunn, J. E., & Gott, J. R., III 1972, ApJ, 176, 1
Hoopes, C. G., Heckman, T. M., Salim, S., et al. 2007, ApJS, 173, 441
Hughes, T. M., Cortese, L., Boselli, A., Gavazzi, G., & Davies, J. I. 2013, A&A, 550, A115
Ignesti, A., Vulcani, B., Botteon, A., et al. 2023, A&A, 675, A118
Izotov, Y. I., Stasińska, G., Meynet, G., Guseva, N. G., & Thuan, T. X. 2006, A&A, 448, 955
Jáchym, P., Sun, M., Kenney, J. D. P., et al. 2017, ApJ, 839, 114
Jauzac, M., Eckert, D., Schwinn, J., et al. 2016, MNRAS, 463, 3876
Jones, T., Sanders, R., Roberts-Borsani, G., et al. 2020, ApJ, 903, 150
Kauffmann, G., Heckman, T. M., Tremonti, C., et al. 2003, MNRAS, 346, 1055
Kewley, L. J., & Ellison, S. L. 2008, ApJ, 681, 1183
Kewley, L. J., Dopita, M. A., Sutherland, R. S., Heisler, C. A., & Trevena, J. 2001, ApJ, 556, 121
Lagattuta, D. J., Richard, J., Clément, B., et al. 2017, MNRAS, 469, 3946
Lah, P., Pracy, M. B., Chengalur, J. N., et al. 2009, MNRAS, 399, 1447
López-Sánchez, Á. R., Dopita, M. A., Kewley, L. J., et al. 2012, MNRAS, 426, 2630
Lotz, J. M., Koekemoer, A., Coe, D., et al. 2017, ApJ, 837, 97
Maiolino, R., Nagao, T., Grazian, A., et al. 2008, A&A, 488, 463
Mannucci, F., Cresci, G., Maiolino, R., Marconi, A., & Gnerucci, A. 2010, MNRAS, 408, 2115
Moretti, A., Poggianti, B. M., Gullieuszik, M., et al. 2018, MNRAS, 475, 4055
Moretti, A., Paladino, R., Poggianti, B. M., et al. 2020, ApJ, 897, L30

Moretti, A., Radovich, M., Poggianti, B. M., et al. 2022, ApJ, 925, 4
Nadolny, J., Lara-López, M. A., Cerviño, M., et al. 2020, A&A, 636, A84
Nakajima, K., Ouchi, M., Isobe, Y., et al. 2023, ApJS, 269, 33
Nedkova, K. V., Häußler, B., Marchesini, D., et al. 2021, MNRAS, 506, 928
Owers, M. S., Randall, S. W., Nulsen, P. E. J., et al. 2011, ApJ, 728, 27
Pagel, B. E. J., Simonson, E. A., Terlevich, R. J., & Edmunds, M. G. 1992, MNRAS, 255, 325
Peña-Guerrero, M. A., Peimbert, A., & Peimbert, M. 2012, ApJ, 756, L14
Pettini, M., & Pagel, B. E. J. 2004, MNRAS, 348, L59
Poggianti, B. M., Fasano, G., Omizzolo, A., et al. 2016, AJ, 151, 78
Poggianti, B. M., Moretti, A., Gullieuszik, M., et al. 2017, ApJ, 844, 48
Poggianti, B. M., Ignesti, A., Gitti, M., et al. 2019a, ApJ, 887, 155
Poggianti, B. M., Gullieuszik, M., Tonnesen, S., et al. 2019b, MNRAS, 482, 4466
Richard, J., Claeyssens, A., Lagattuta, D., et al. 2021, A&A, 646, A83
Rosales-Ortega, F. F., Sánchez, S. F., Iglesias-Páramo, J., et al. 2012, ApJ, 756, L31
Salpeter, E. E. 1955, ApJ, 121, 161
Sánchez, S. F., Rosales-Ortega, F. F., Jungwiert, B., et al. 2013, A&A, 554, A58
Sánchez, S. F., Barrera-Ballesteros, J. K., López-Cobá, C., et al. 2019, MNRAS, 484, 3042
Sanders, R. L., Shapley, A. E., Kriek, M., et al. 2015, ApJ, 799, 138
Shipley, H. V., Lange-Vagle, D., Marchesini, D., et al. 2018, ApJS, 235, 14
Stasińska, G. 2002, in Revista Mexicana de Astronomia y Astrofisica Conference Series, eds. W. J. Henney, J. Franco, & M. Martos, 12, 62
Sun, M., Donahue, M., Roediger, E., et al. 2010, ApJ, 708, 946
Sutherland, R. S., & Dopita, M. A. 1993, ApJS, 88, 253
Tomičić, N., Vulcani, B., Poggianti, B. M., et al. 2021, ApJ, 922, 131
Tonnesen, S., & Bryan, G. L. 2012, MNRAS, 422, 1609
Tonnesen, S., & Bryan, G. L. 2021, ApJ, 911, 68
Tonnesen, S., Bryan, G. L., & Chen, R. 2011, ApJ, 731, 98
Tremonti, C. A., Heckman, T. M., Kauffmann, G., et al. 2004, ApJ, 613, 898
Treu, T., Roberts-Borsani, G., Bradac, M., et al. 2022, ApJ, 935, 110
Vale Asari, N., Couto, G. S., Cid Fernandes, R., et al. 2019, MNRAS, 489, 4721
Vogt, F. P. A., Dopita, M. A., Borthakur, S., et al. 2015, MNRAS, 450, 2593
Werle, A., Cid Fernandes, R., Vale Asari, N., et al. 2019, MNRAS, 483, 2382
Werle, A., Poggianti, B., Moretti, A., et al. 2022, ApJ, 930, 43
Yao, Y., Chen, G., Liu, H., et al. 2022, A&A, 661, A112
Zahid, H. J., Dima, G. I., Kudritzki, R.-P., et al. 2014, ApJ, 791, 130

Appendix A: Additional figures

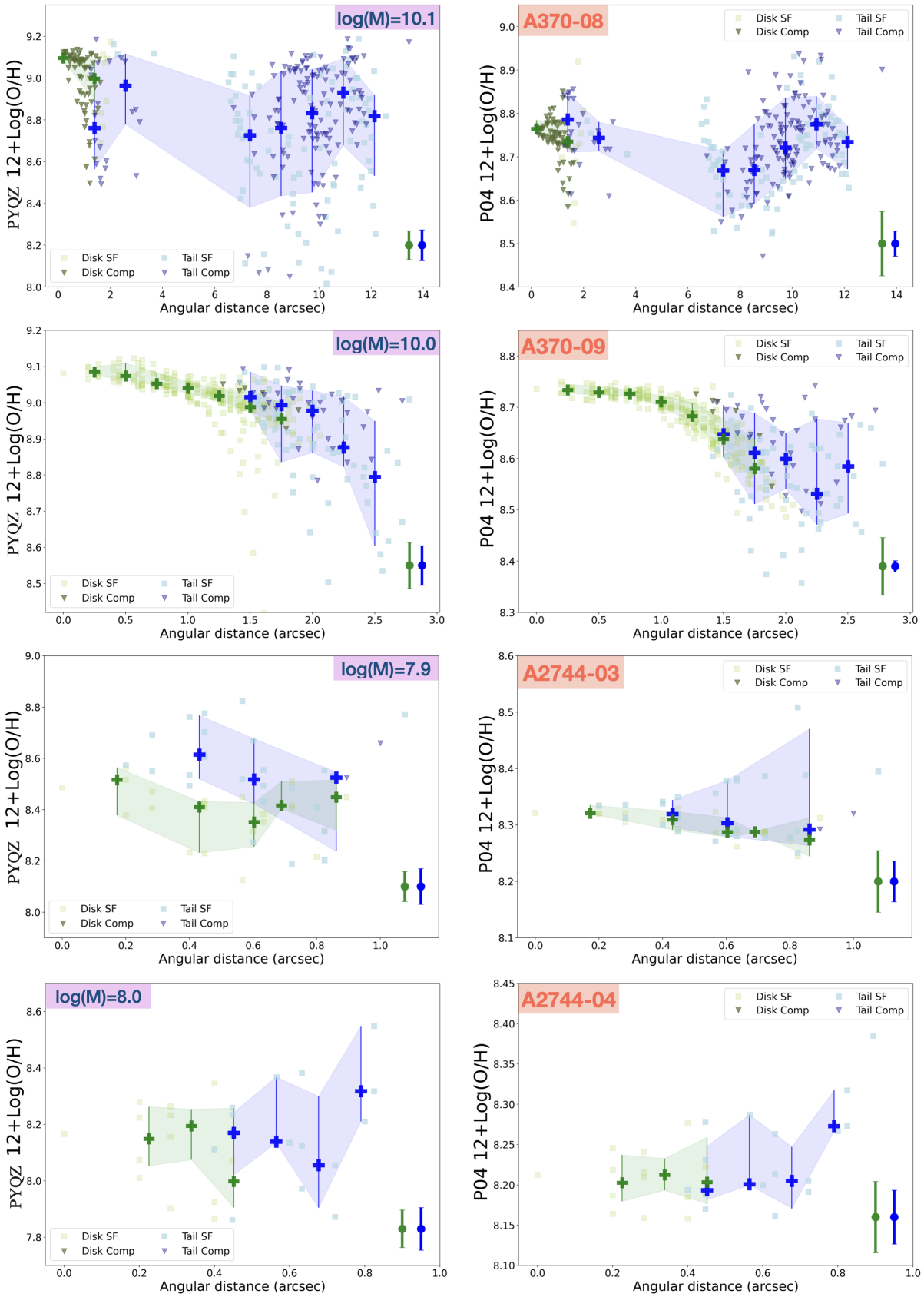

Fig. A.1. continued.

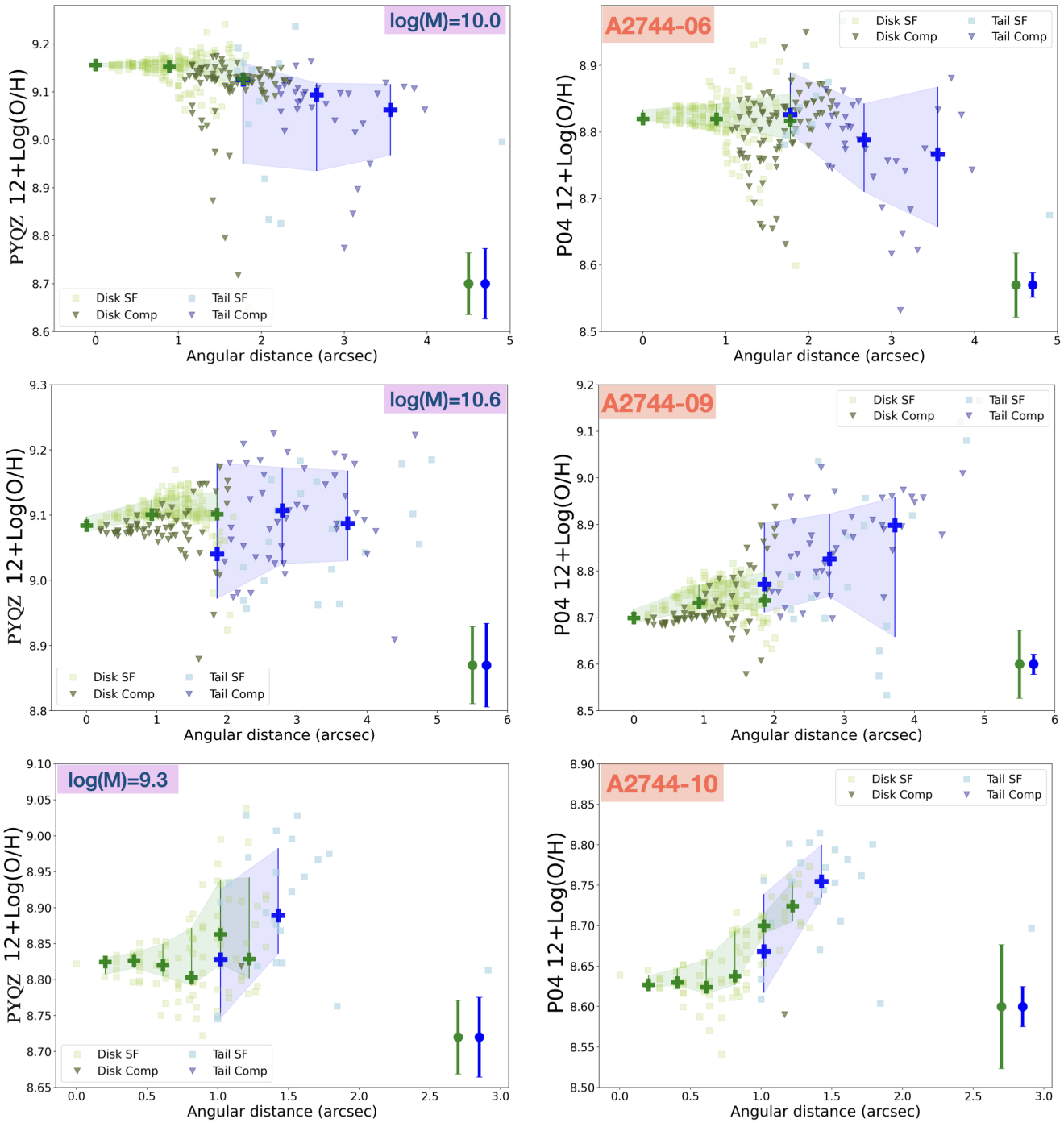

Fig. A.2. continued.

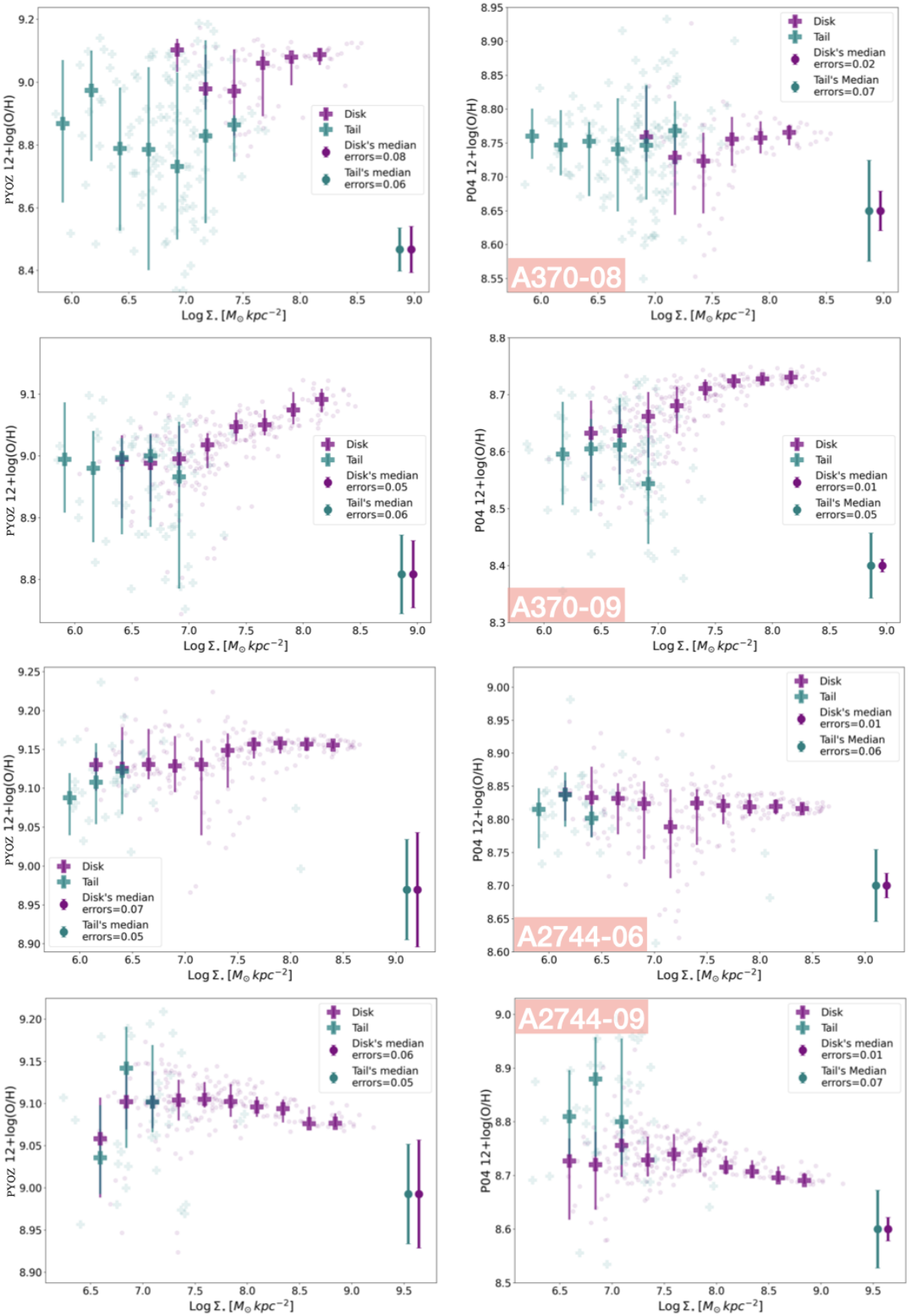

Fig. A.3. continued.